Geophysical Research Letter

Supporting Information for

Ambiguity in Recent Changes to US Methane Emissions

Leyang Feng[1], Sakineh Tavakkoli[2], Sarah M. Jordaan[2], Arlyn E. Andrews[3], Joshua S. Benmergui[4], Darryn W. Waugh[5], Mingyang Zhang[1], Dylan C. Gaeta[1], and Scot M. Miller[1]

[1]Department of Environmental Health and Engineering, Johns Hopkins University, Baltimore, MD

[2]School of Advanced International Studies, Johns Hopkins University, Washington, DC

[3]Global Monitoring Laboratory, Earth System Research Laboratories, NOAA, Boulder, CO

[4]John A. Paulson School of Engineering and Applied Sciences, Harvard University, Boston, MA

[5]Department of Earth & Planetary Sciences, Johns Hopkins University, Baltimore, MD

Contents of this file

S1 Additional details on trend line fitting for in-situ observations and GOSAT

This section of the supplement provides detailed steps of trend line fitting for in-situ and GOSAT observations using modeled MMR. Specifically, we fit trend lines at each in-situ observation site for each scenario. As in Lan et al. (2019), we fit a linear trend line using ordinary least squares (OLS) to monthly model estimates that have been deseasonalized using a 2nd-order polynomial fit and band pass filter. The data are further log10 transformed before line fitting (If the model output were to increase by a constant percentage per annum, the resulting output would have a non-linear slope, and the log10 transformation would make that slope linear.). For GOSAT, we first average the model output into 4° by 4° latitude-longitude grid boxes across CONUS and estimate a trend for each grid box, the same procedure as Sheng et al. (2018). GOSAT sounding locations are sparsely distributed and vary from month-to-month, and this averaging procedure yields a more consistent MMR estimate for each grid box. We deseasonalize the model outputs using seasonal-trend-loess (STL) decomposition method (Cleveland et al. 1990), and fit a trend-line to annually-averaged model outputs using OLS.

S2 Additional details on the analysis for in-situ monitoring sites

This section of the supplement provides additional analysis of the model outputs at in situ atmospheric monitoring sites: detailed model time series at each site, comparisons against trends in observed atmospheric mixing ratios, and additional comparisons against individual meteorological variables.

Figures S1 - S8 display time series of MMR at each in situ observation site and for each modeling scenario (i.e., scenarios 1-4). Each figure displays monthly-averaged model outputs that have been deseasonalized, as described in Sect. 2.2. In addition, the figures show the trend line fitted to the modeled time series for each scenario. The time series show a clear upward trend in MMR at most observation sites (at least for several model scenarios), providing a visual confirmation of the trend lines reported in Fig. 1

The figures further show observed methane enhancements (deseasonalized and interpolated for gap-filling, shown in black) and a trend line fitted to these observed enhancements. The model outputs often do a good job of reproducing monthly variability in the observations, even if the model outputs do not always match the magnitude of the observations. Note that the purpose of this study is not to determine which of the modeled scenarios is the best match against observations. Rather, the four scenarios developed here are used as test cases to explore the plausible impacts of meteorology and emissions. By contrast, trends in observed atmospheric methane are likely due to a combination of both meteorological factors and complex, unknown trends in surface emissions. We feel that the latter are best estimated using Bayesian inverse modeling, which is beyond the scope of this manuscript.

Note that in Figs. S1-S8, the fitted trend lines for observed methane enhancements (shown in black) for a few sites exhibits a slight downward trend (i.e., site BAO, WBI, and WGC). We find that such downward trends are likely due to a reduction in observation frequency. Figs. S9-S11 display the timeseries with fitted trend lines of observed, monthly-averaged methane enhancements (shown in black), deseasonalized observed methane enhancements (shown in blue), and monthly observation frequency (grey bars in the background). All three sites (BAO, WBI, and WGC) show a downward shift in the timeseries associated with a change in observation frequency: these timeseries show an upward trend before 2011 and after 2011 but exhibit a downward shift in 2011. Such reduction in observations can cause observation sites to capture less variability in atmospheric methane within a given month, especially sporadic methane spikes from nearby cities or other sources, and can result in fitting unrealistic downward trends.

Also note that the observed methane enhancements displayed in Figs. S1-S8 show mixing ratios after subtracting a modeled methane background or boundary condition. The methane boundary condition used here approximates methane mixing ratios in air over the Pacific and Atlantic Oceans before these air masses enter the United States. The purpose of this study is to explore methane trends across the US, not global trends, and subtracting the methane boundary condition removes the influence of global methane trends from the analysis. By contrast, we do not need to subtract a boundary condition from the model simulations; the STILT simulations here are regional in scope and only model atmospheric methane enhancements due to fluxes in North America.

We use the methane boundary condition generated for NOAA's CarbonTracker-Lagrange project for all simulations in this study. This approach is identical to that used in multiple existing methane and GHG modeling studies based on the STILT model (e.g., Hu et al. 2019; Miller et al. 2013, 2014, 2016; Shiga et al. 2018a, 2018b). Specifically, we first interpolate in situ methane observations zonally and in time to create an interpolated "curtain" of estimated methane values across the Pacific and Atlantic oceans (e.g., as in Jeong et al. 2013 and Miller et al. 2013). We then sample this curtain at the ending locations and times of the particles in each STILT simulation. For each STILT simulation, we then average the sampled curtain values across all 500 particles in the simulation, and this average value becomes the estimated background for a specific methane observation.

Further note that we do not include methane oxidation in either the methane boundary condition calculations or in the calculation of STILT footprints. This approach is similar to other studies of regional methane emissions that use a particle trajectory model like STILT (e.g., Cui et al. 2015, 2017; Huang et al. 2019; Miller et al. 2013, 2014, 2016a, 2016b; Ren et al. 2018; Sargent et al. 2021). The atmospheric lifetime of methane is 12 years, while the particles in each STILT simulation are allowed to travel backward in time for 10 days (though many trajectories terminate at the edge of the North American model domain in less time). Over 10 days, up to 0.2 – 0.3% of modeled methane could decay, and we therefore do not include this chemistry in model simulations due to its small impact. Furthermore, even large inter-annual variability in hydroxyl radical (OH) levels would likely have minimal impact on the model simulations here given their regional scope.

Figures S12 – S14 provide additional detail on the comparisons between annual-averaged, modeled MMR and various meteorological parameters (i.e., planetary boundary layer (PBL) height, vertical wind speed (Ω), and total wind speed at the observation location). These figures display each comparison as a scatterplot, whereas Fig. 4 in the main article lists the estimated correlation coefficient for each comparison. These figures provides visual confirmation that the comparison between MMR and local wind speed is often stronger than the comparisons between MMR and other meteorological parameters.

Figures S15 – S17 further compare observed methane enhancements against the meteorological parameters described above. Fig. 4 in the main article displays this comparison for modeled methane outputs while the figure here shows the same comparison for observed methane enhancements. Similar to the model analysis in Fig. 4, we also find that the relationships between observed methane enhancements and meteorology are often strongest for local wind speed. This result provides further confirmation of the analysis in Fig. 4.

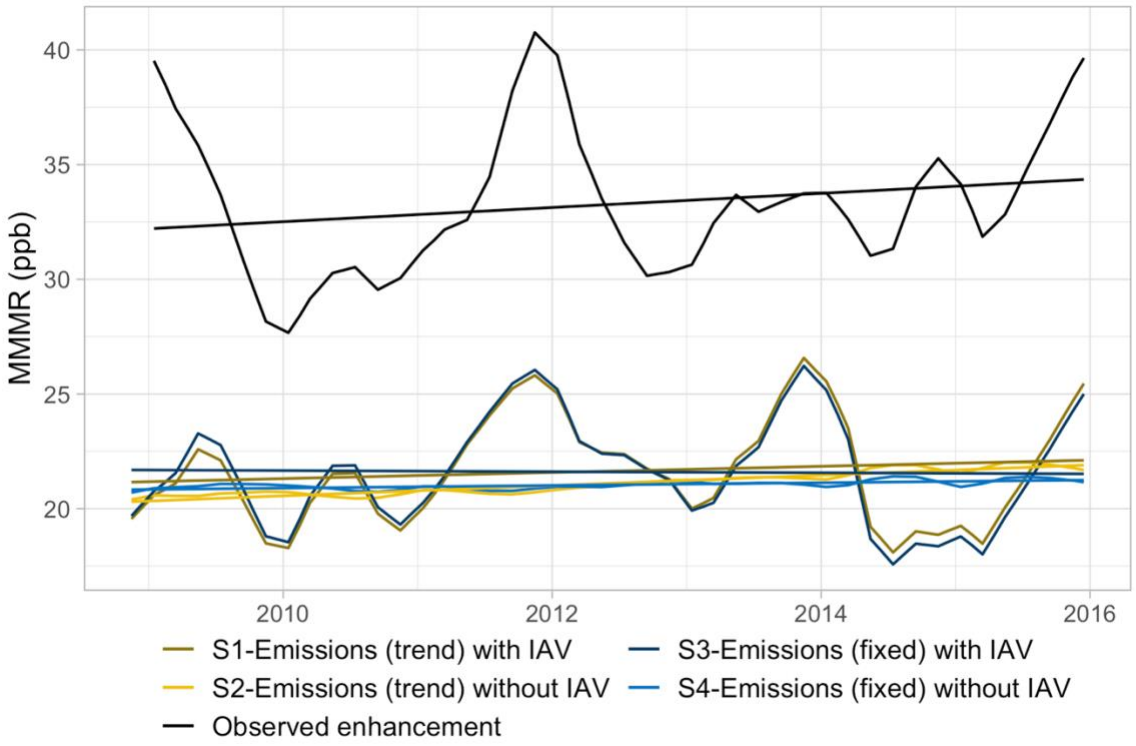

Figure S1. Time series of MMR at site AMT for all 4 modeling scenarios and observed trends

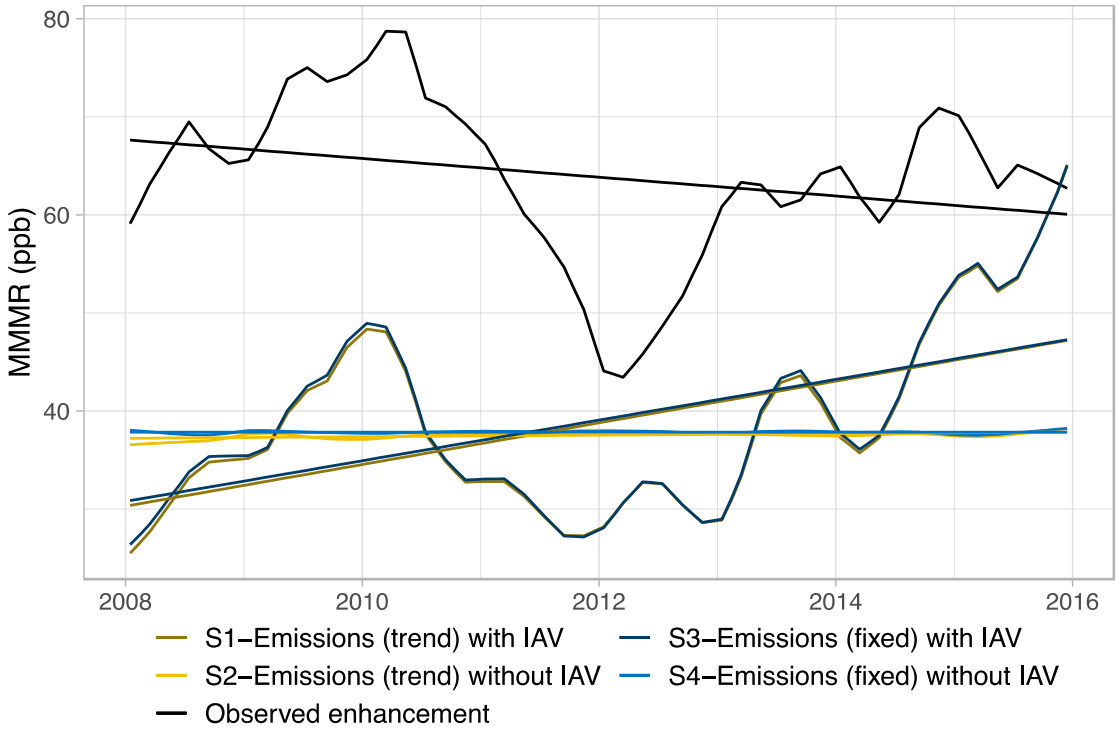

Figure S2. Time series of MMR at site BAO for all 4 modeling scenarios and observed trends

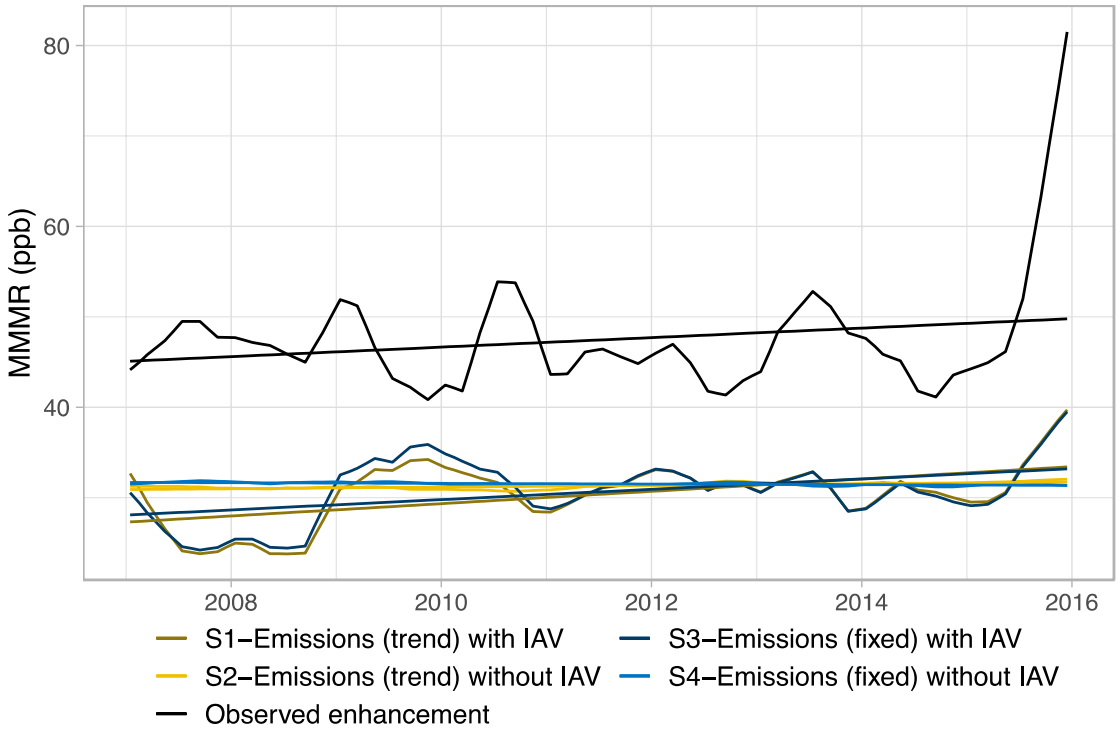

Figure S3. Time series of MMR at site LEF for all 4 modeling scenarios and observed trends

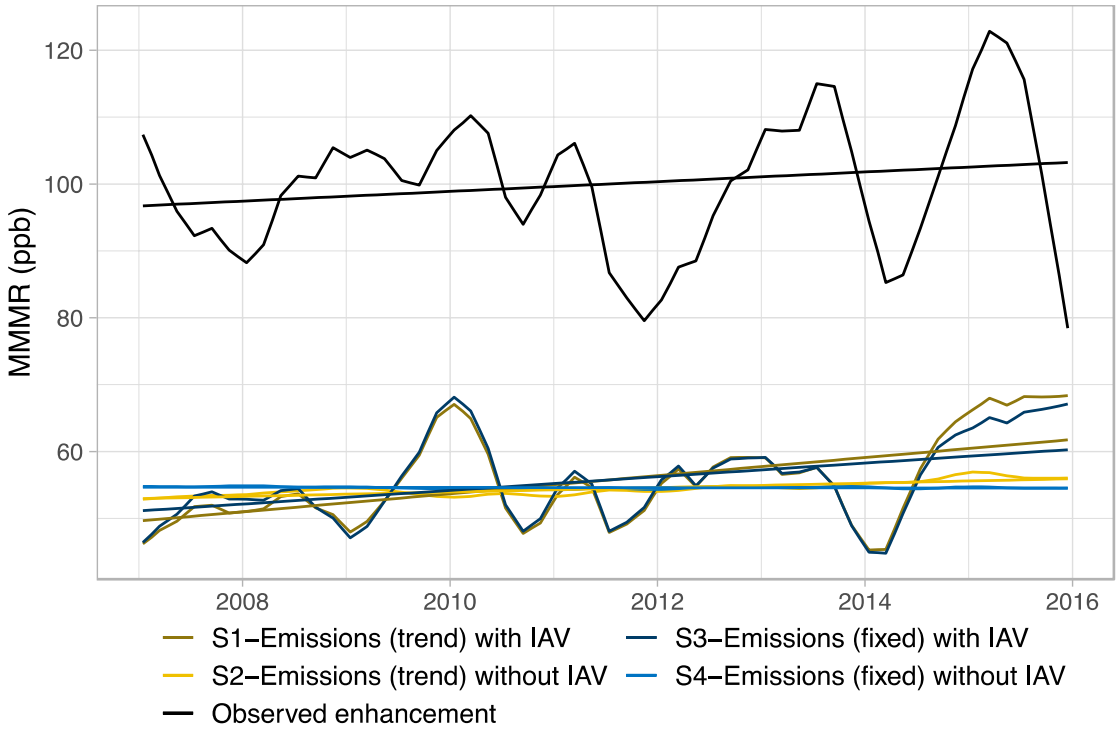

Figure S4. Time series of MMR at site SGP for all 4 modeling scenarios and observed trends

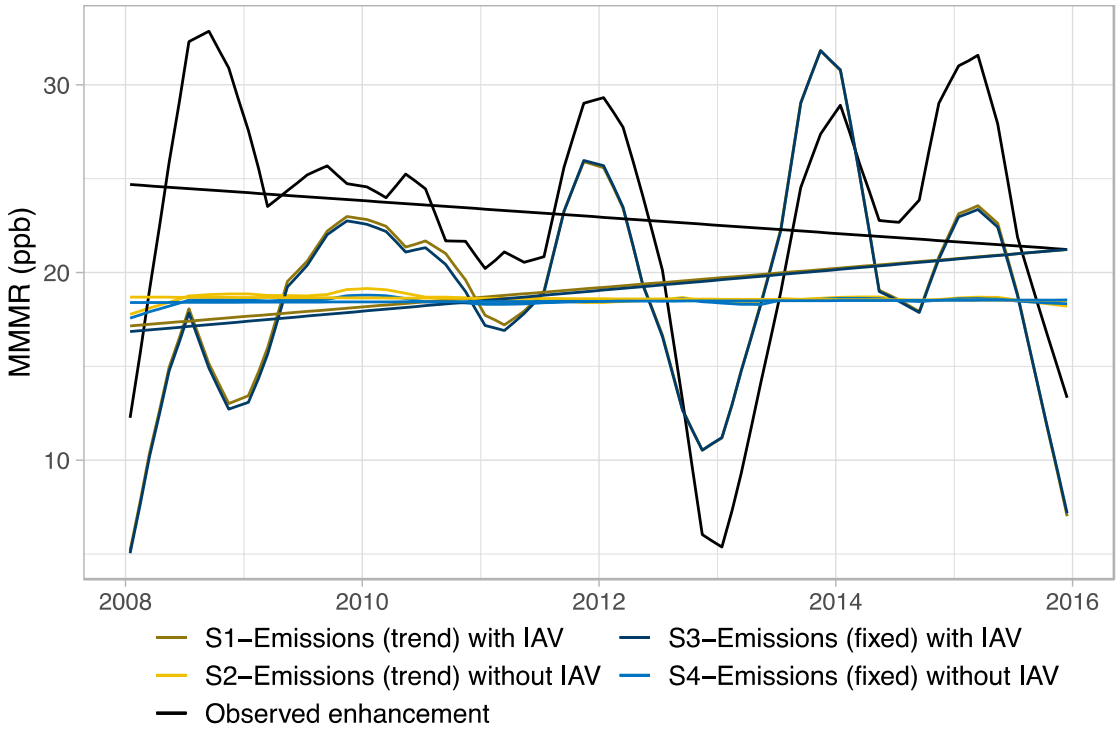

Figure S5. Time series of MMR at site STR for all 4 modeling scenarios and observed trends

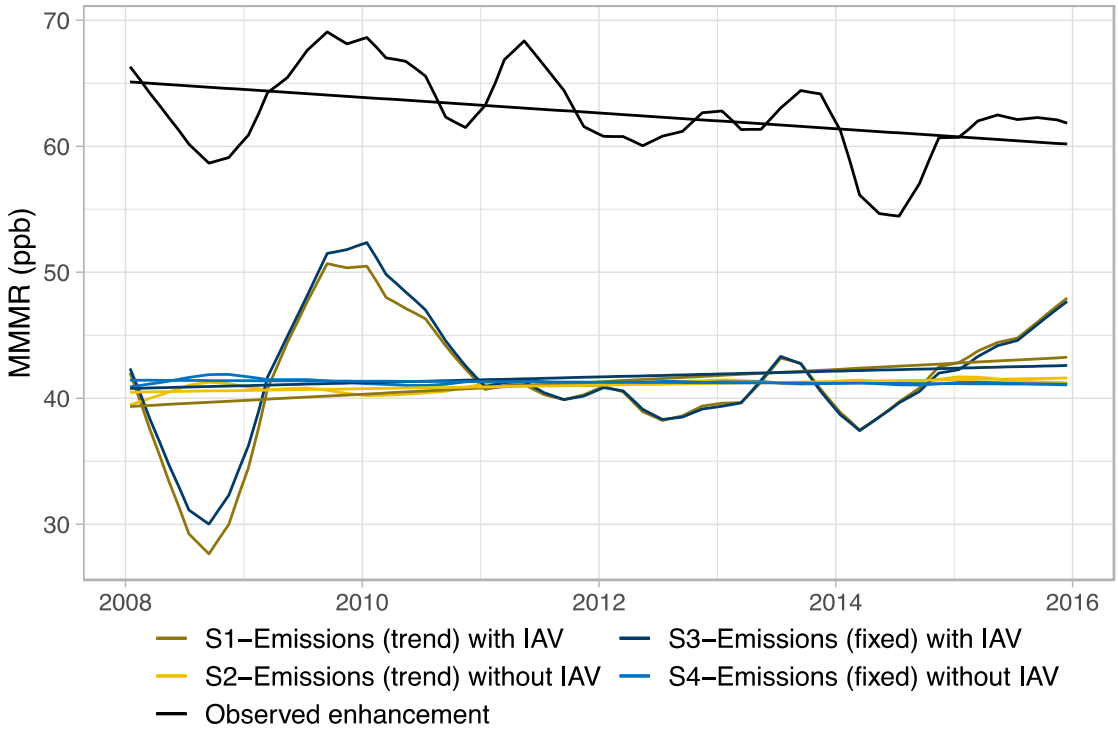

Figure S6. Time series of MMR at site WBI for all 4 modeling scenarios and observed trends

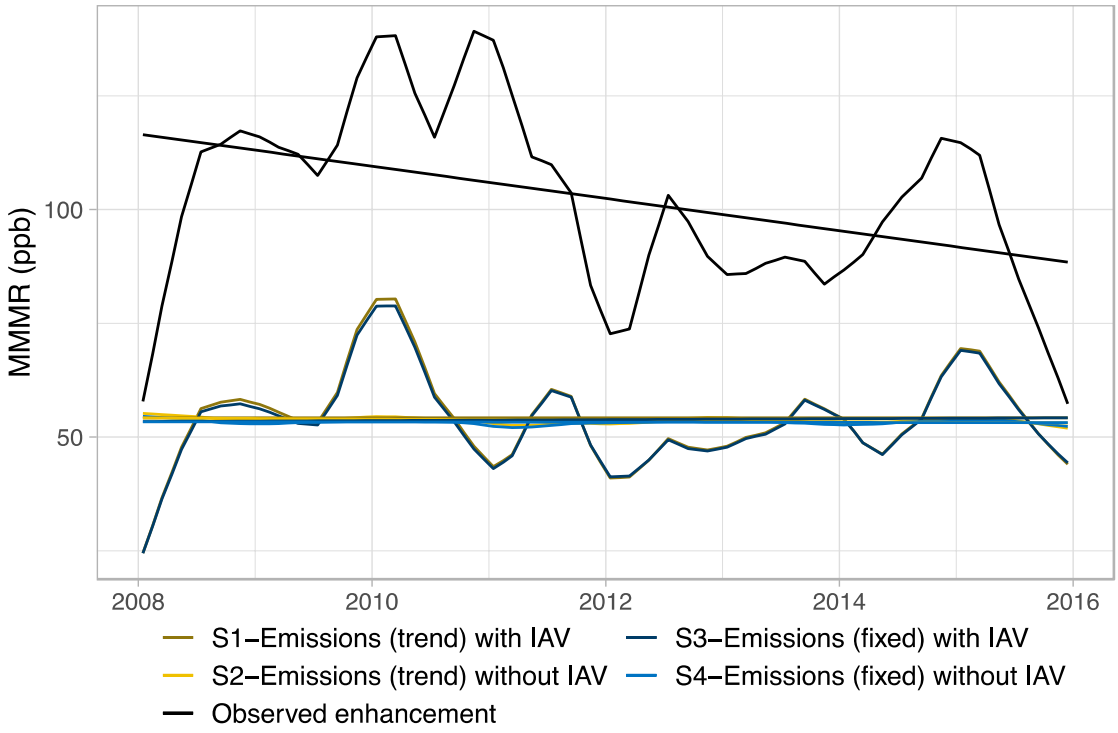

Figure S7. Time series of MMR at site WGC and for all 4 modeling scenarios and observed trends

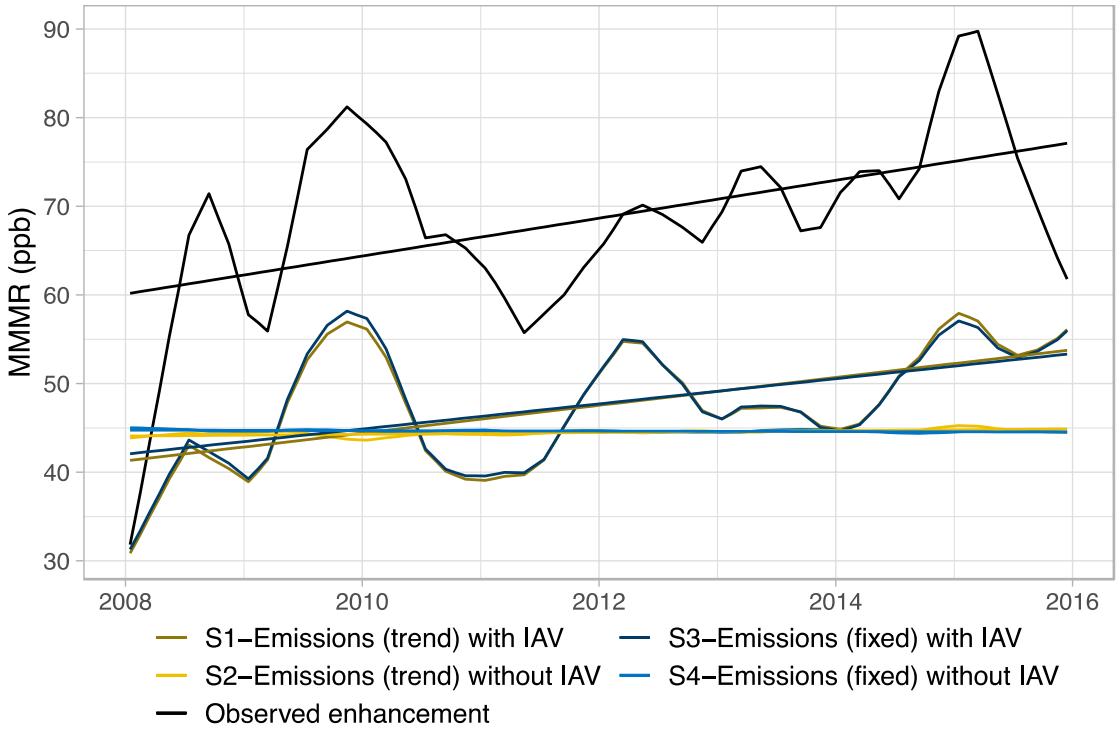

Figure S8. Time series of MMR at site WKT for all 4 modeling scenarios and observed trends

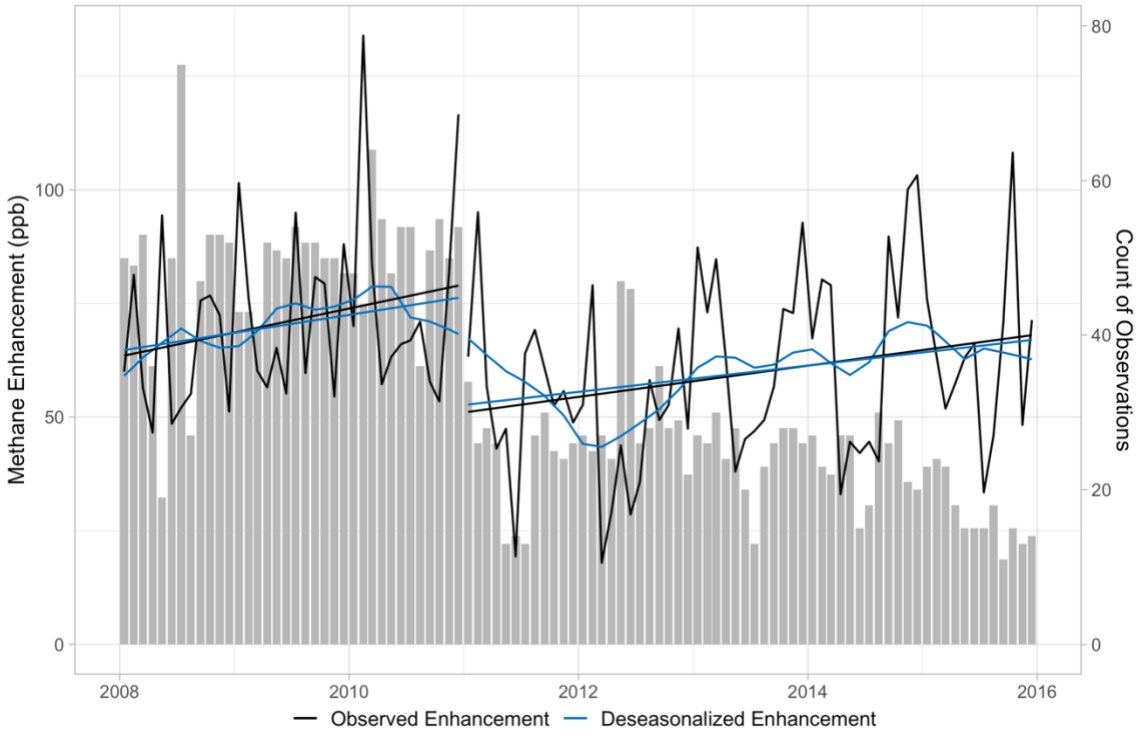

Figure S9. Observed methane enhancement at site BAO with observation frequency

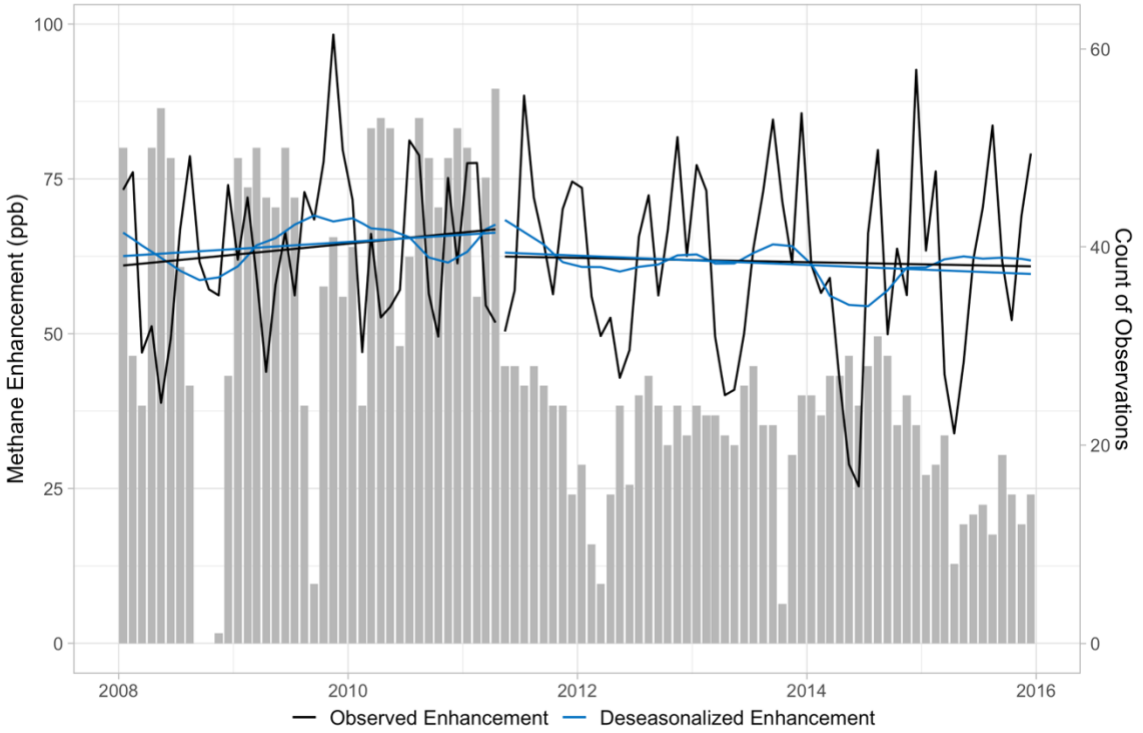

Figure S10. Observed methane enhancement at site WBI with observation frequency

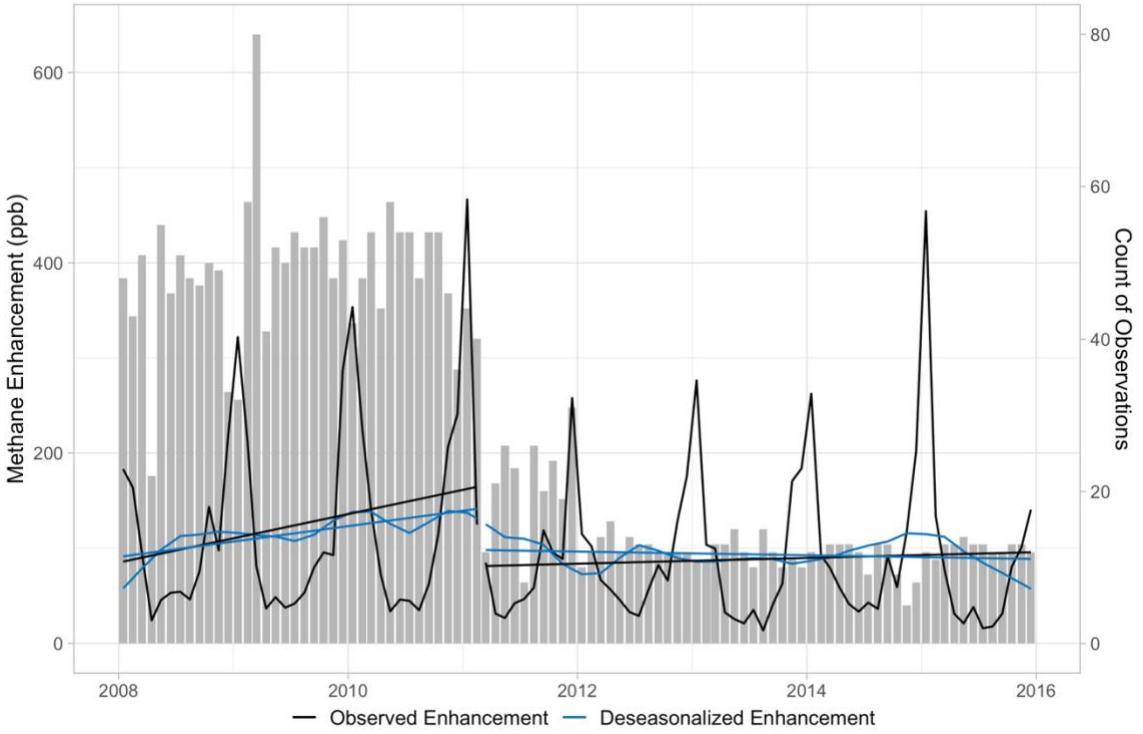

Figure S11. Observed methane enhancement at site WGC with observation frequency

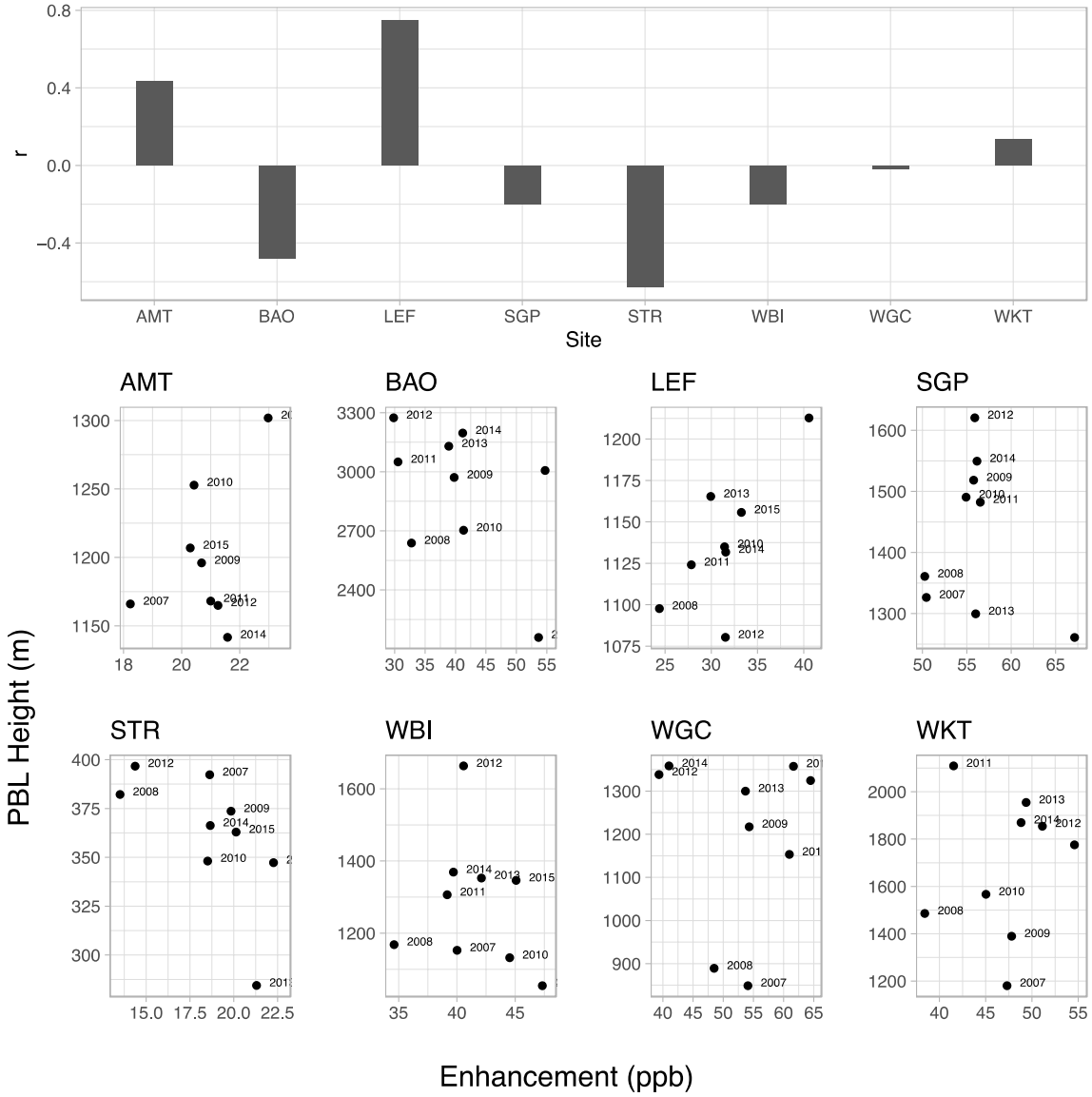

Figure S12. Correlation coefficient between modeled MMR and PBL height parameters for all in-situ monitoring sites.

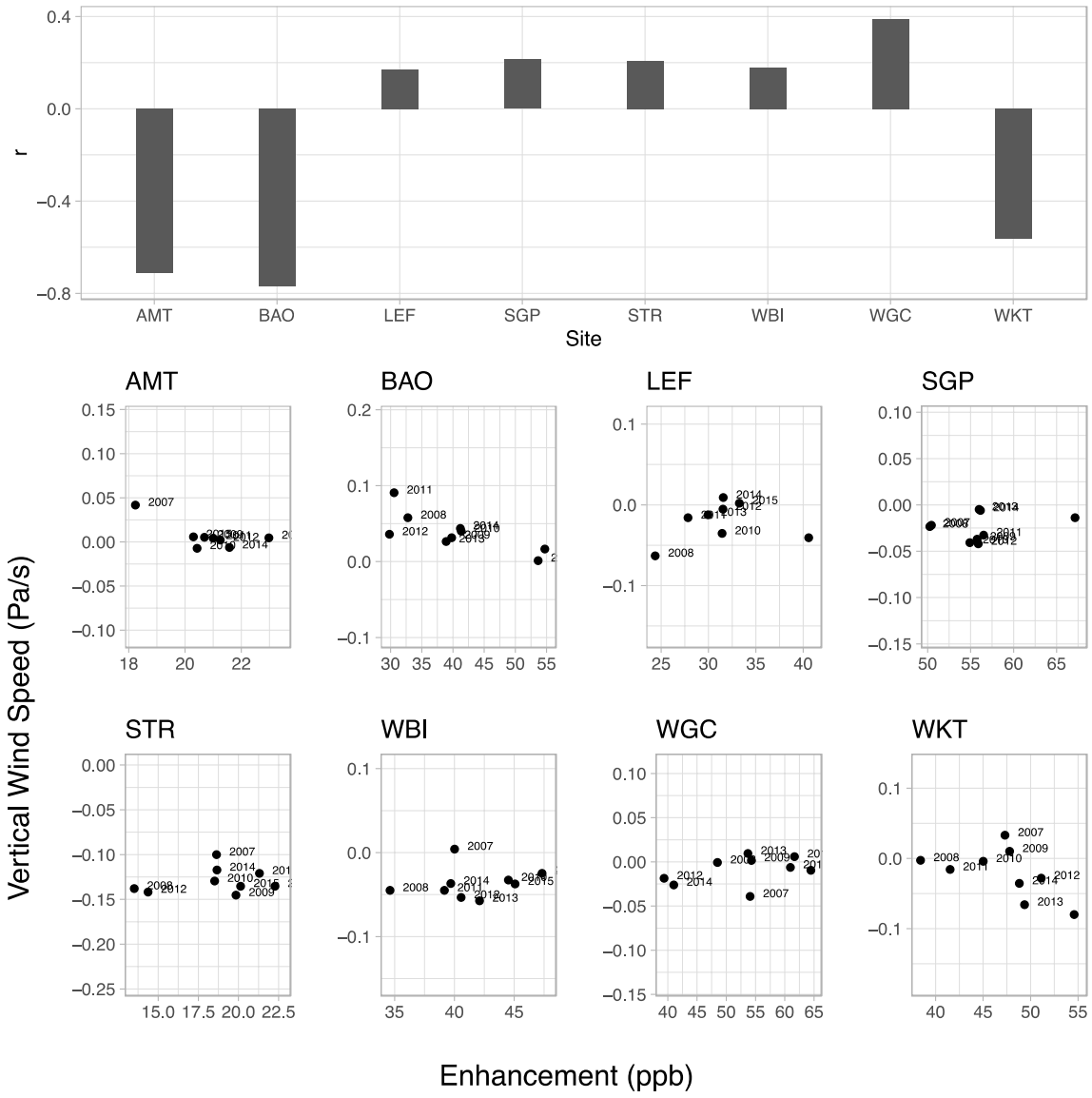

Figure S13. Correlation coefficient between modeled MMR and vertical wind speed for all in-situ monitoring sites.

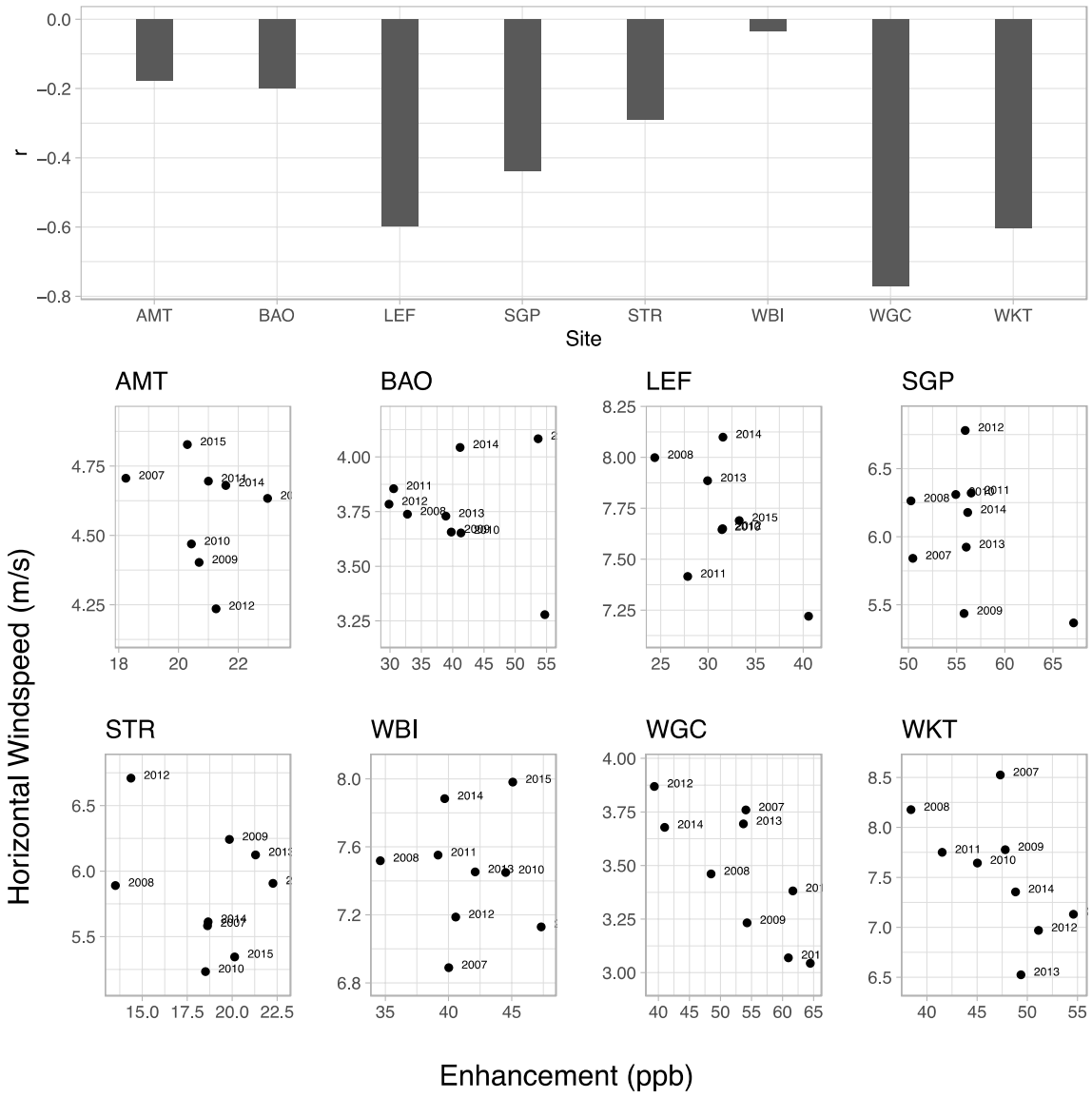

Figure S14. Correlation coefficient between modeled MMR and horizontal windspeed for all in-situ monitoring sites.

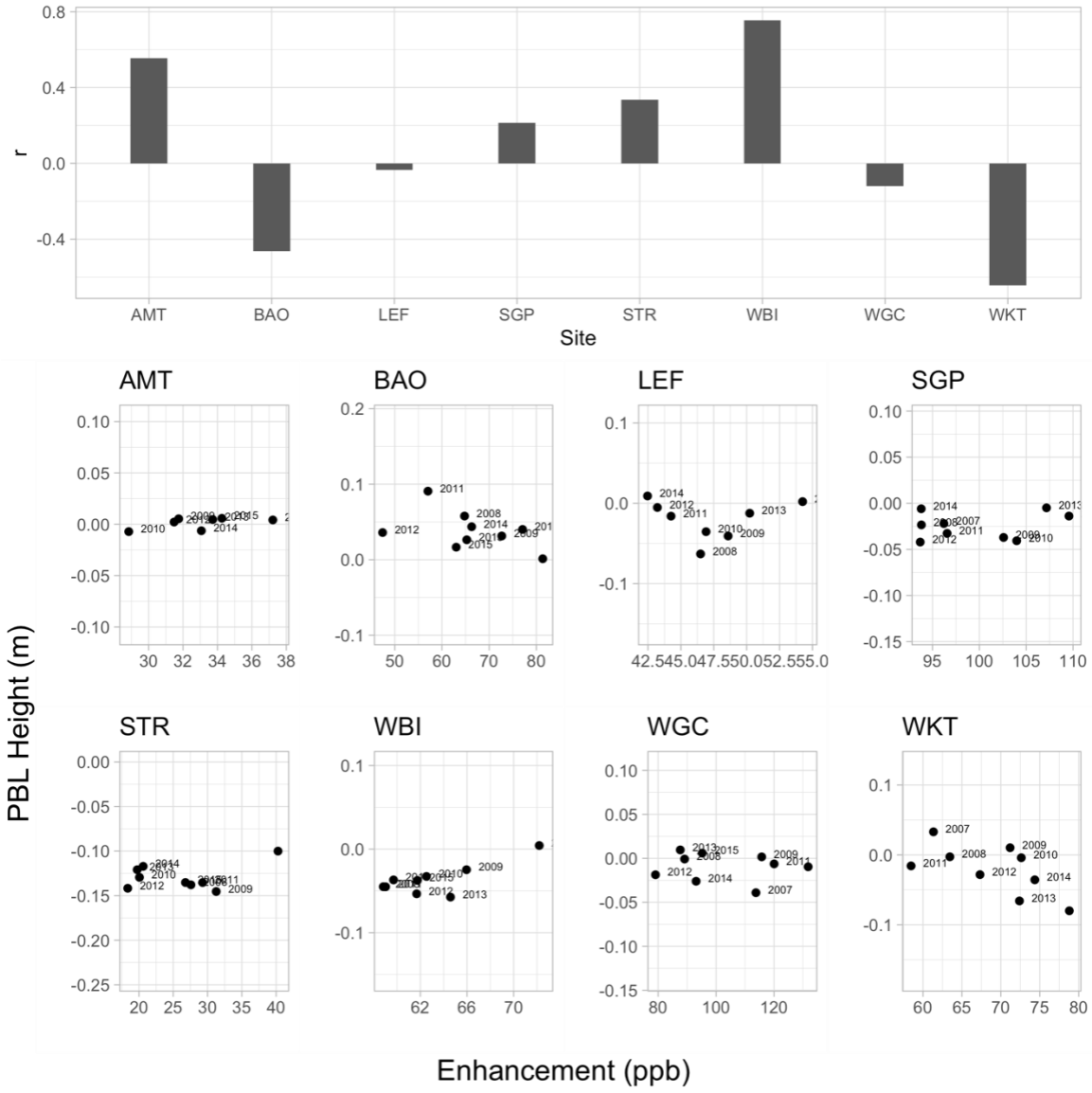

Figure S15. Correlation coefficient between observed MMR and PBL height for all in-situ monitoring sites.

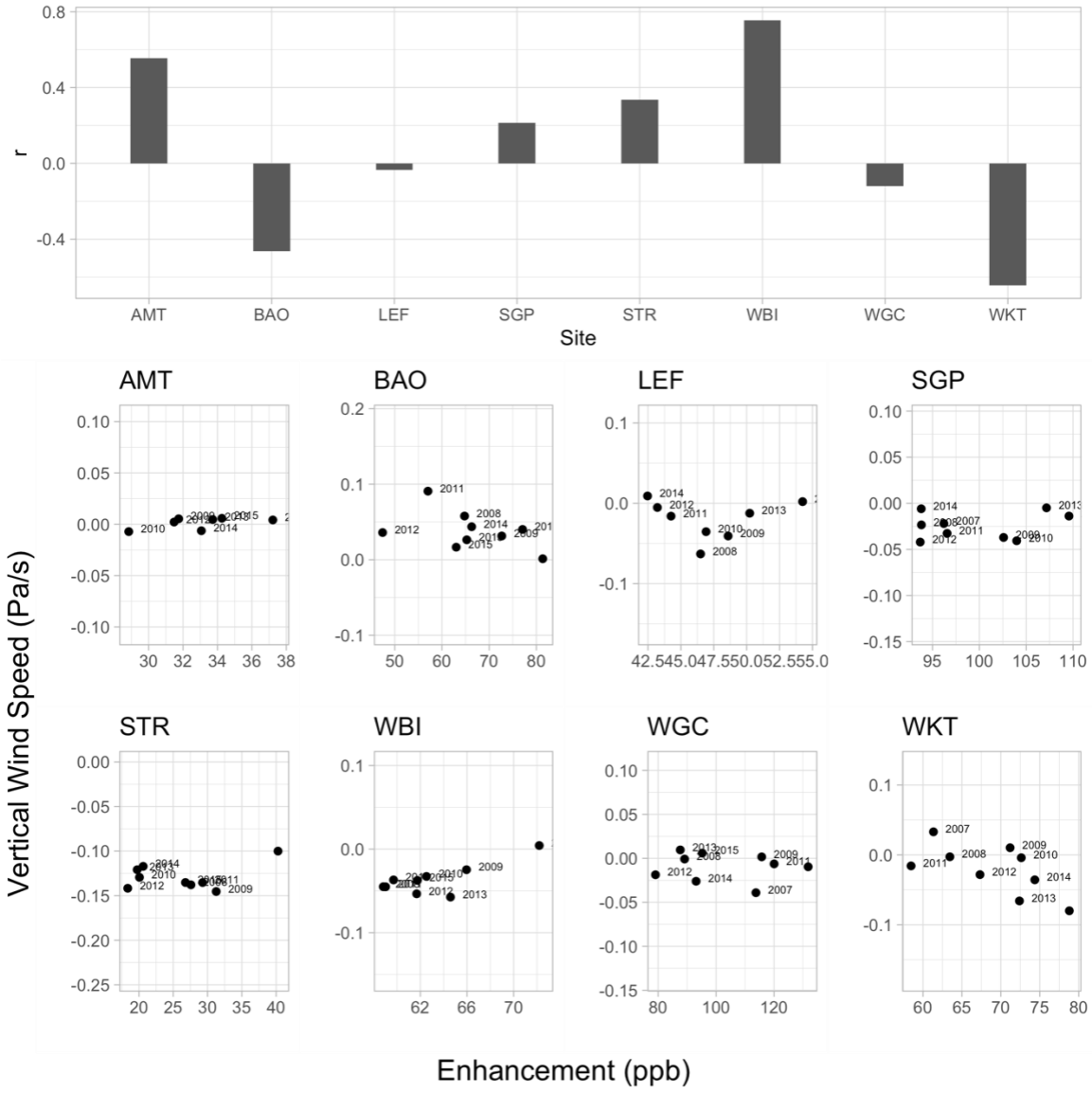

Figure S16. Correlation coefficient between observed MMR and vertical windspeed for all in-situ monitoring sites.

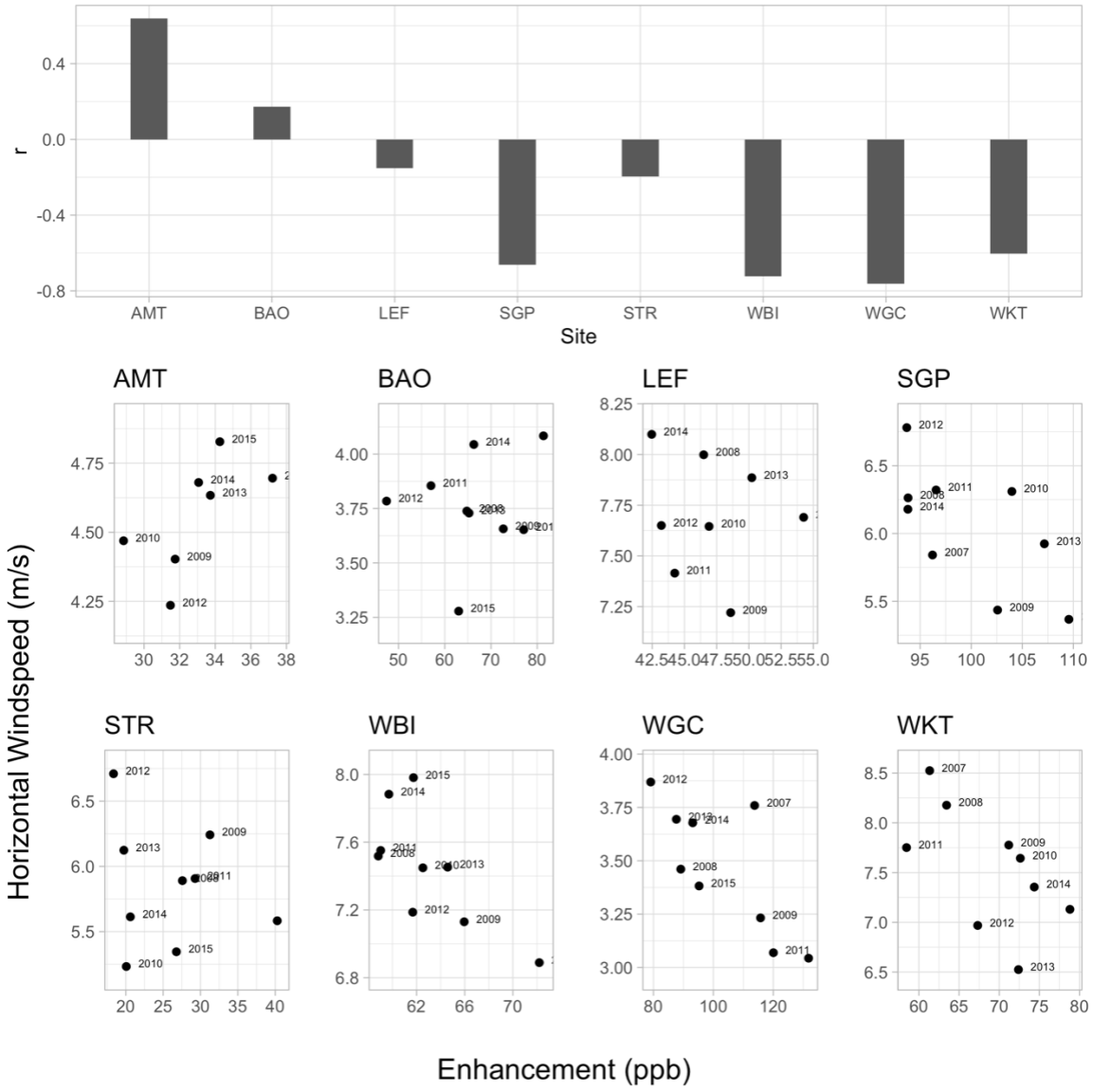

Figure S17. Correlation coefficient between observed MMR and horizontal windspeed for all in-situ monitoring sites.

S3 Additional details on the analysis for GOSAT observations

This section includes supplementary figures describing analysis of the GOSAT observations and the associated model simulations. Figures S18-S21 display the trends in modeled MMR at GOSAT observation locations, averaged into 4° by 4° latitude-longitude grid boxes. These figures display the results for all four of the modeling scenarios, in contrast to Fig. 2 in the main article, which only displays the results for scenario three (no trend in emissions, IAV in meteorology). Figures S18-S21 show that the simulated trend in emissions yields a relatively small change in the model outputs; the trends in MMR for scenario one (trend in emissions, IAV in meteorology) are similar to the trends in MMR estimated for scenario three (no trend in emissions, IAV in

meteorology). Similarly, the estimated trends in scenario two (trend in emissions, no IAV in meteorology) are similar to the estimated trends in scenario four (no trend in emissions, no IAV in meteorology). By contrast, the largest difference among simulations (i.e., the largest difference in the estimated trends) is between scenarios that do and do not include IAV in meteorology. Specifically, scenarios one and three, which include IAV in meteorology, are most different from scenarios two and four, which do not include IAV in meteorology. This analysis using GOSAT observations parallels the conclusions of the analysis for the in-situ observation sites; trends in emissions have a modest impact on trends in MMR while IAV in meteorology has a much larger impact.

Figures S22 - S28 further display modeled MMR time series at several prototypical locations (i.e., for several 4° by 4° latitude-longitude grid boxes). These figures provide visualization of the model and observational outputs that are used in trend fitting. Each figure displays annually-averaged MMR for each modeling scenario, and trend lines fitted to each of these model time series. These figures further reinforce the large differences between model simulations that do and do not include IAV in meteorology (e.g., scenarios one and three versus two and four).

Note that we also subtract a methane background or boundary condition from the GOSAT observations before plotting the time series in Figures S22 - S28 and before fitting a trendline, as in Fig. 2. By subtracting a background or boundary condition, we remove global methane trends from the analysis and focus only on trends over North America. We construct this methane background using the same approach as in Sheng et al. (2018). Specifically, within each year and each 4° by 4° grid box, we identify the GOSAT observations with the lowest observed mixing ratios (the lowest 5th percentile). We then average those observations in the lowest 5th percentile and use this average as the methane background for that year in that grid box. Sheng et al. (2018) used this approach to calculating the background because multiple existing studies have used similar percentile approaches for estimating regional backgrounds (e.g., Goldstein et al. 1995).

The approach used to estimate the background for GOSAT observations is not the same as the approach used for in situ observations in this study (Sect. S1). We do so for multiple reasons. First, we want to directly compare against existing studies of methane emissions from North America and have therefore used the same approach for GOSAT and in situ observations, respectively, as in existing studies (e.g., Jeong et al. 2013, Miller et al. 2013, and Sheng et al. 2018). Second, there is always a possibility that GOSAT observations may exhibit biases relative to in situ observations. We therefore use GOSAT observations to build the background for the GOSAT analysis and in situ observations to build the background for the in-situ analysis. This approach ensures that any discrepancies between in situ and satellite observations do not contaminate the estimated background.

The final set of figures associated with this section of the supplement provides more in-depth visualization of the relationship between MMR and the magnitude of the local footprint (Fig. S29-S35). In the main article, we argue that local meteorological processes are likely driving IAV in MMR at the GOSAT observation sites. We argue this point in the main article by exploring correlations between MMR and the annually-averaged

magnitude of the local footprint (Fig. 3). Note that we define the local footprint as a 4° latitude/longitude radius area around the observation location. Figures S29-S35 show scatter plots comparing MMR and the magnitude of the local footprint for several prototypical locations. In Fig. 3, we find that MMR and the magnitude of the local footprint are closely correlated at most locations. The scatterplots shown here further confirm that point.

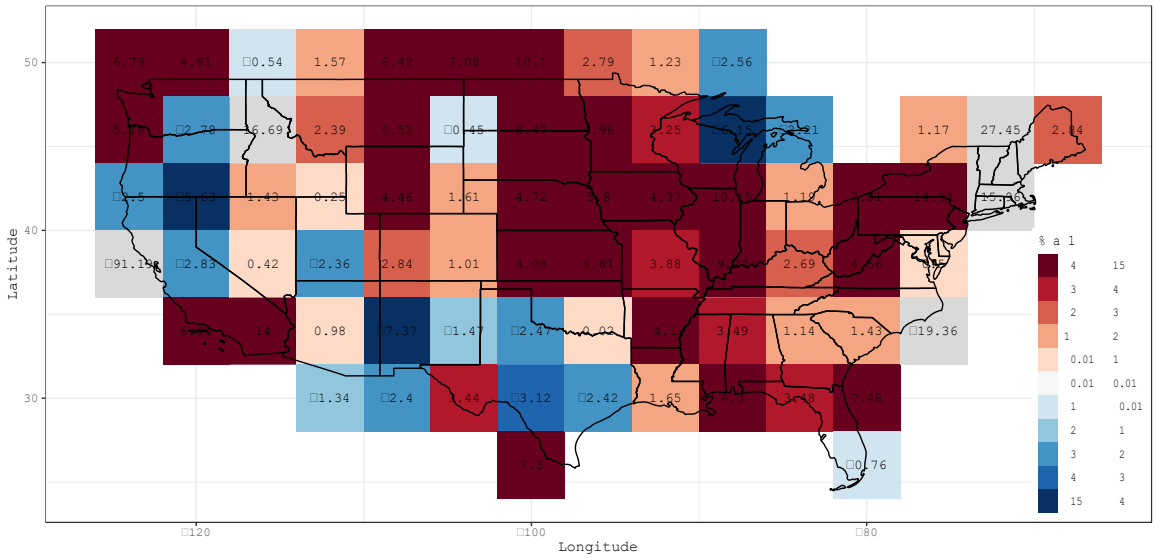

Figure S18. Modeled MMR trends using GOSAT observations for scenario 1

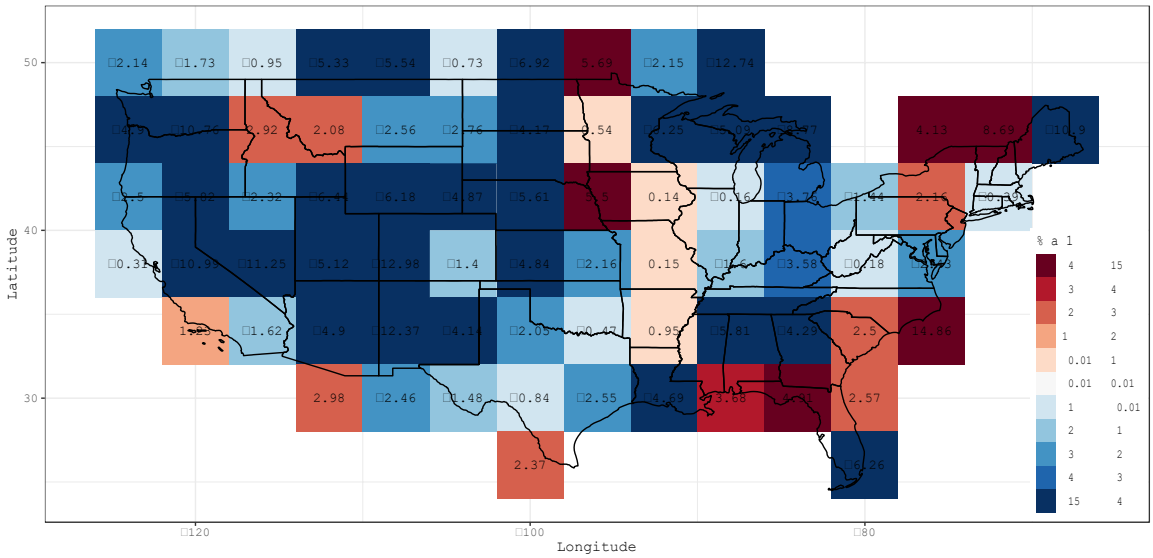

Figure S19. Modeled MMR trends using GOSAT observations for scenario 2

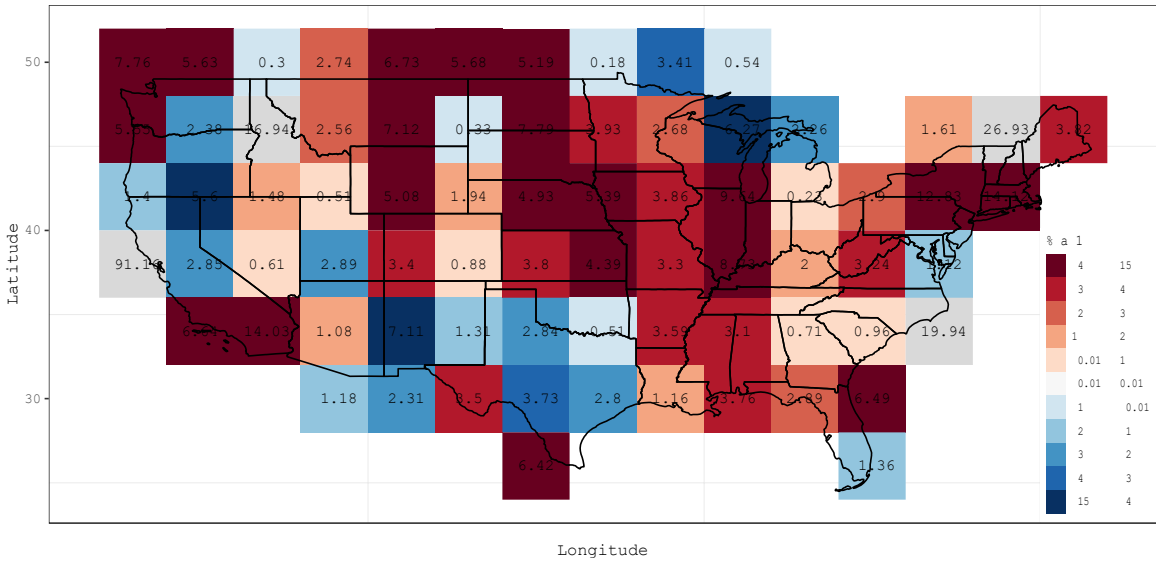

Figure **S20.** Modeled MMR trends using GOSAT observations for scenario 3

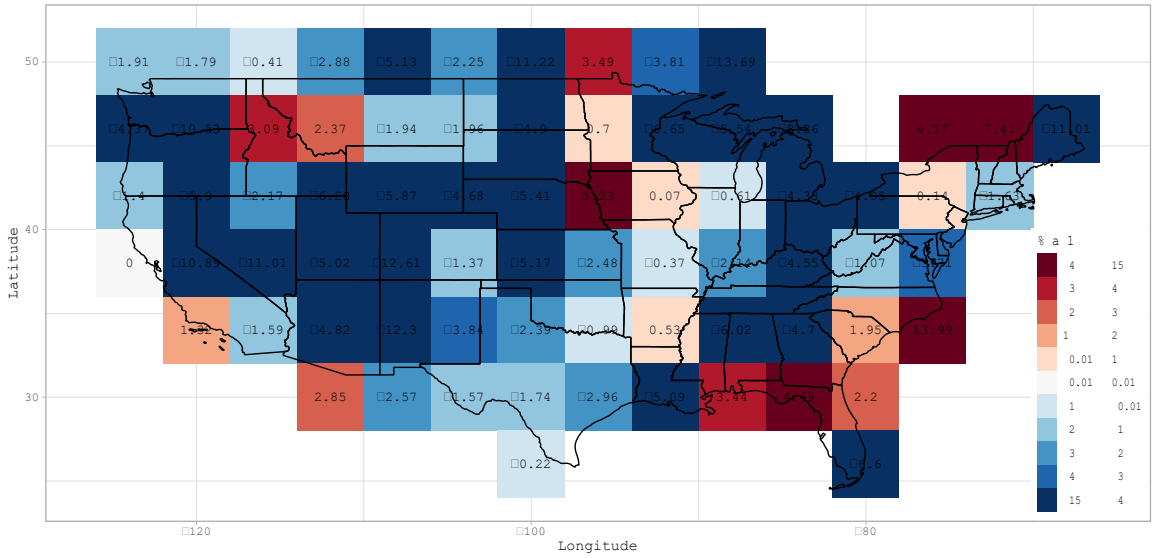

Figure S21. Modeled MMR trends using GOSAT observations for scenario 4

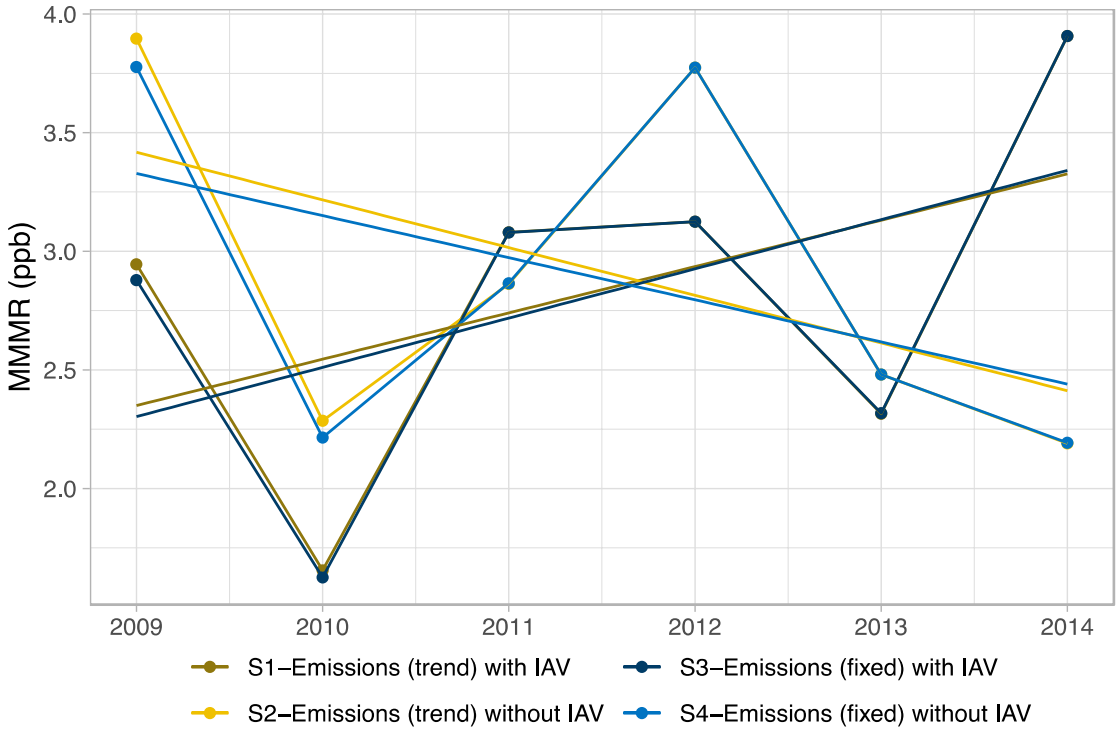

Figure S22. Time series of MMR for GOSAT prototypical location 1 (West Washington State)

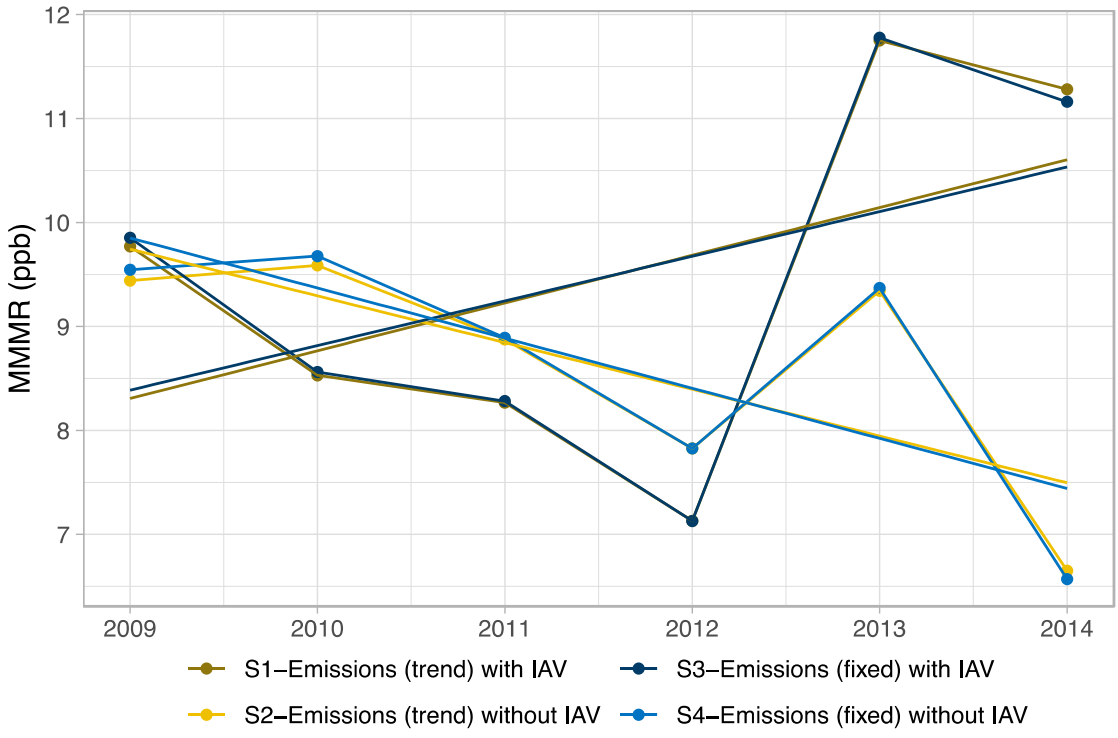

Figure S23. Time series of MMR for GOSAT prototypical location 2 (West Kansas)

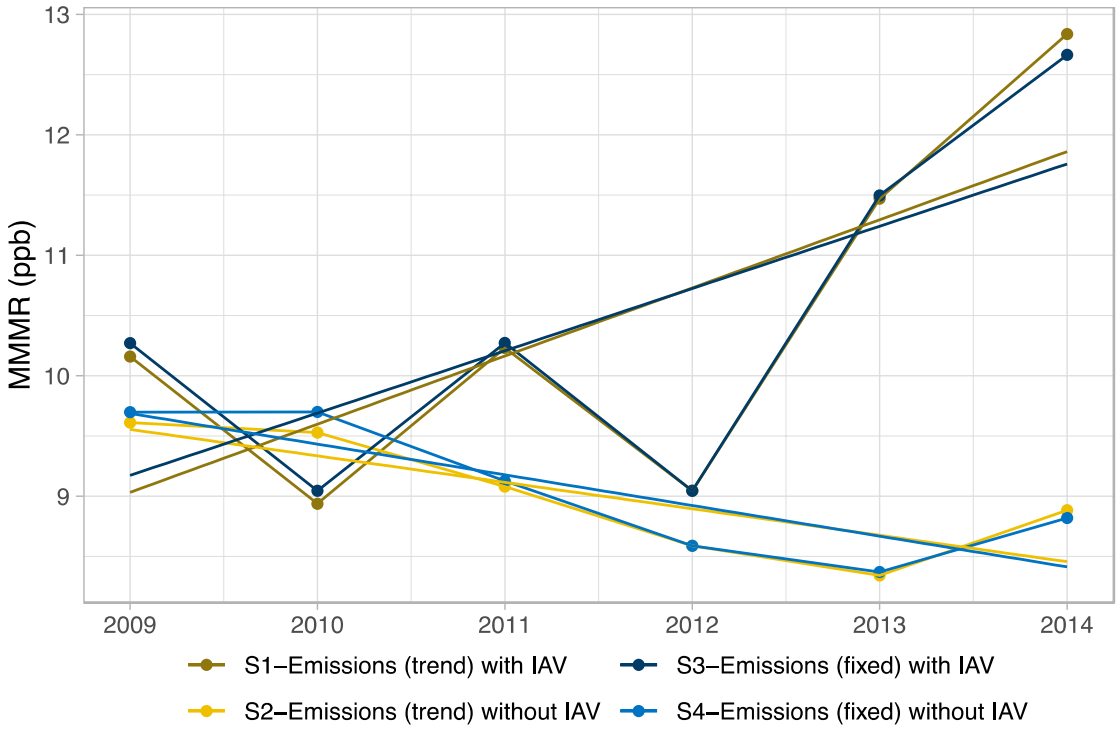

Figure S24. Time series of MMR for GOSAT prototypical location 3 (East Kansas)

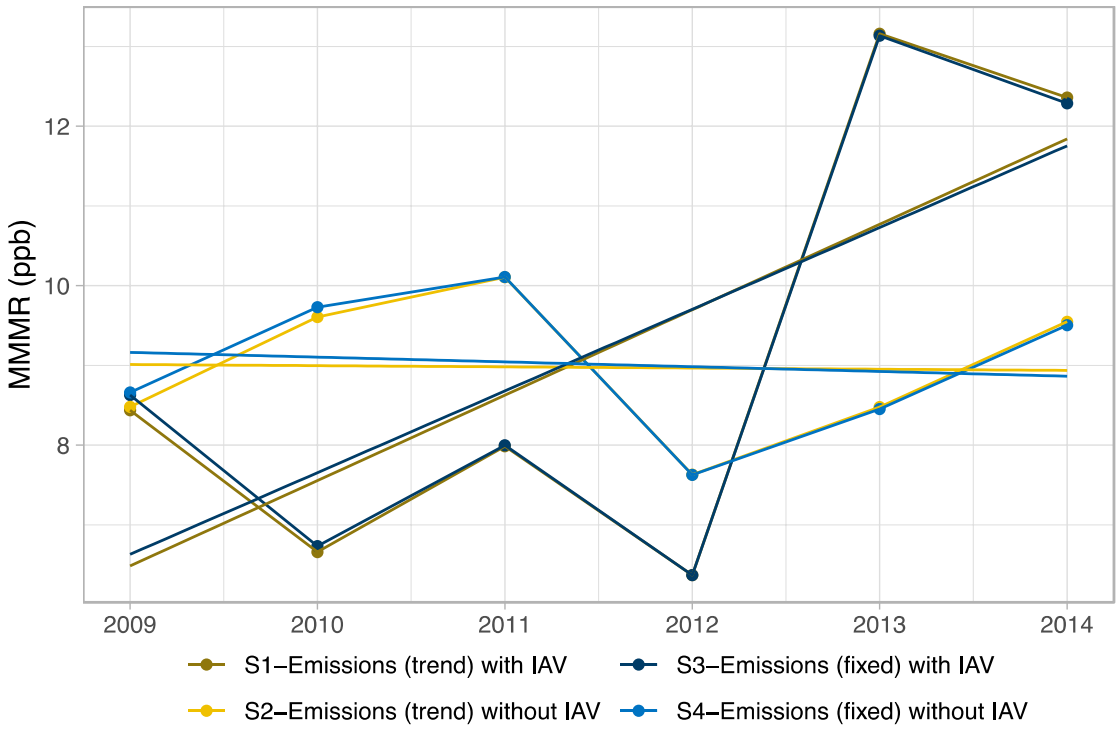

Figure S25. Time series of MMR for GOSAT prototypical location 4 (Chicago area)

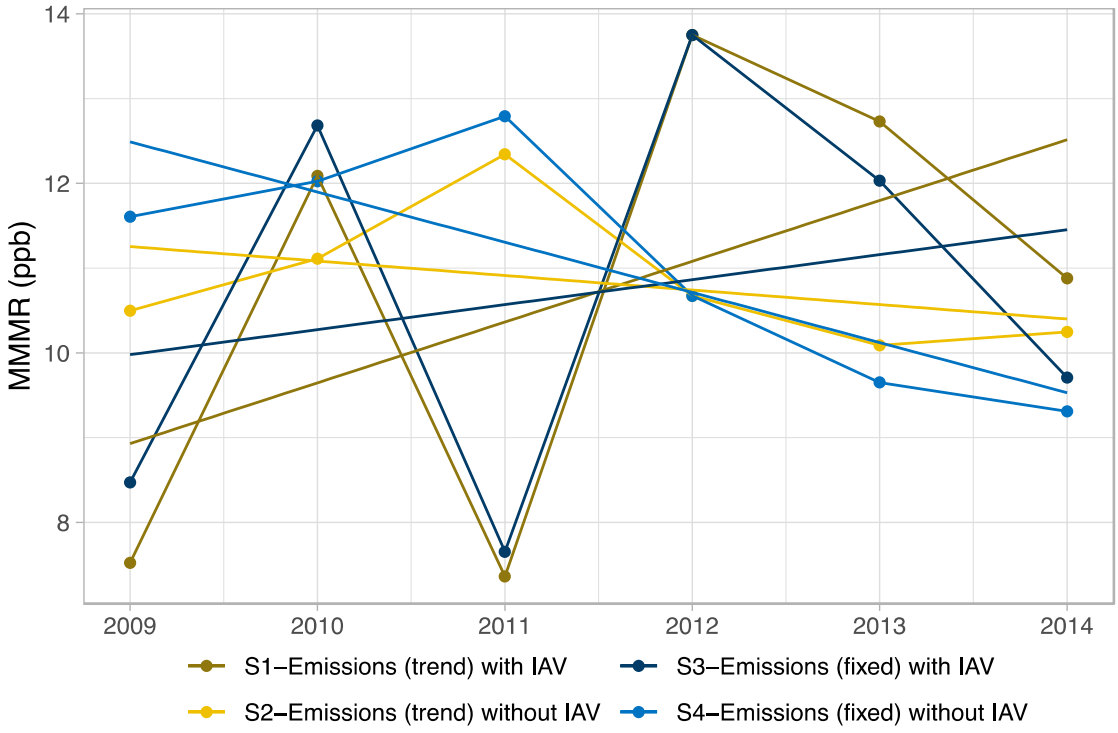

Figure S26. Time series of MMR for GOSAT prototypical location 5 (West New York - West Pennsylvania)

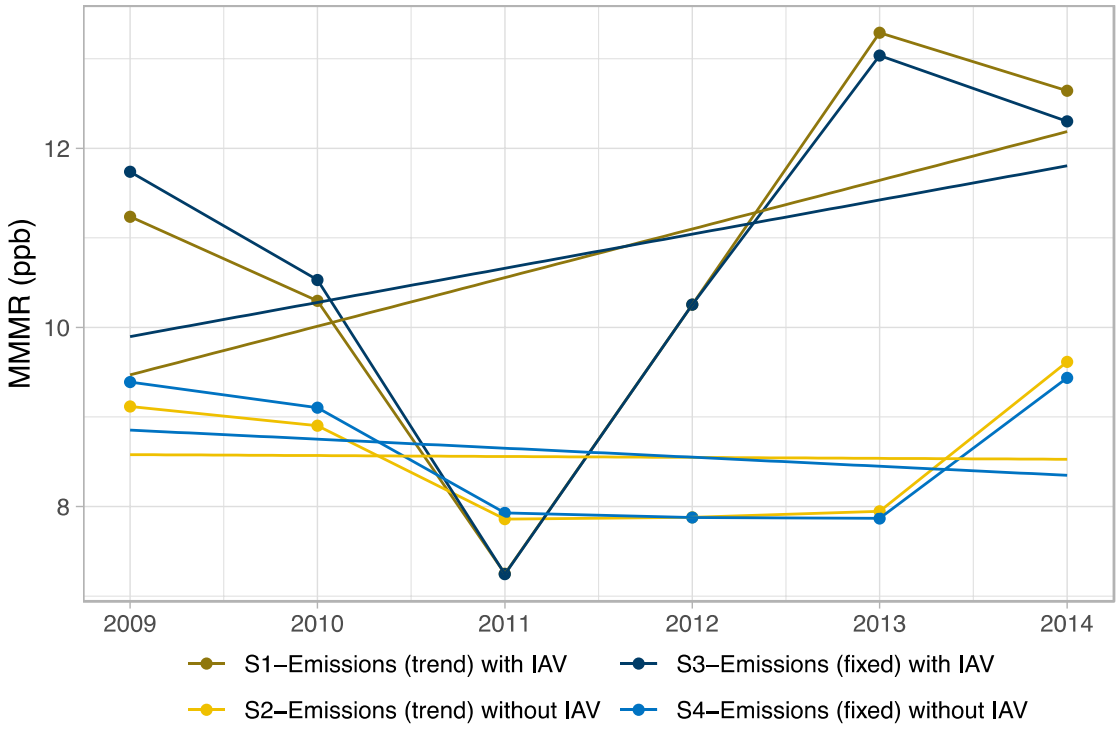

Figure S27. Time series of MMR for GOSAT prototypical location 6 (West Virginia - Southwest Virginia)

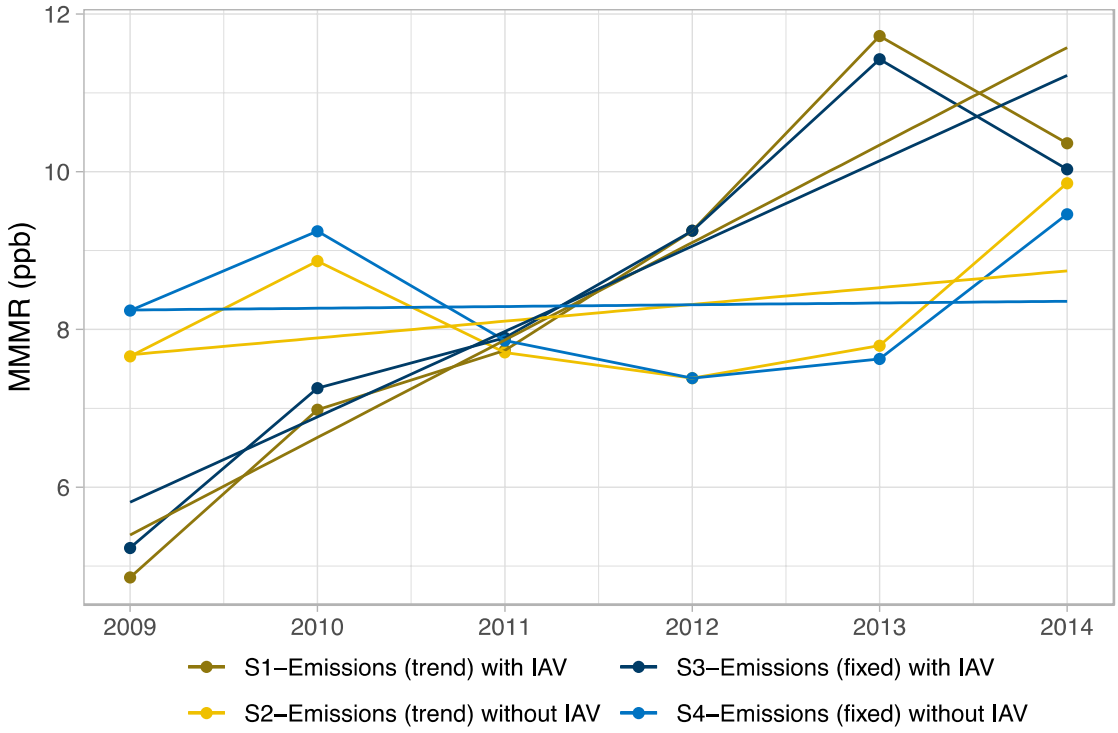

Figure S28. Time series of MMR for GOSAT prototypical location 7 (East New York - East Pennsylvania)

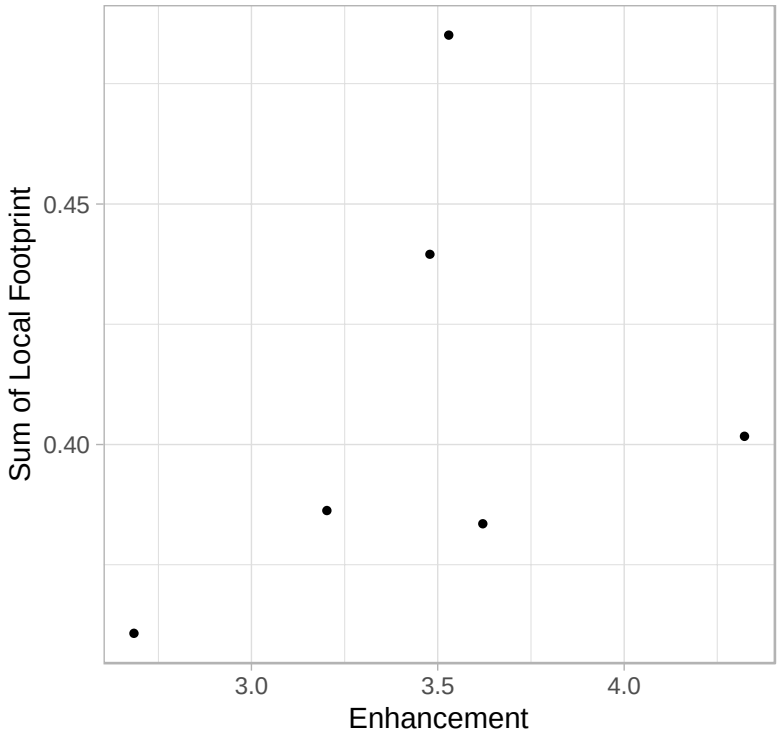

Figure S29. Scatter plot of total modeled enhancement vs. local footprints for GOSAT prototypical location 1 (West Washington State)

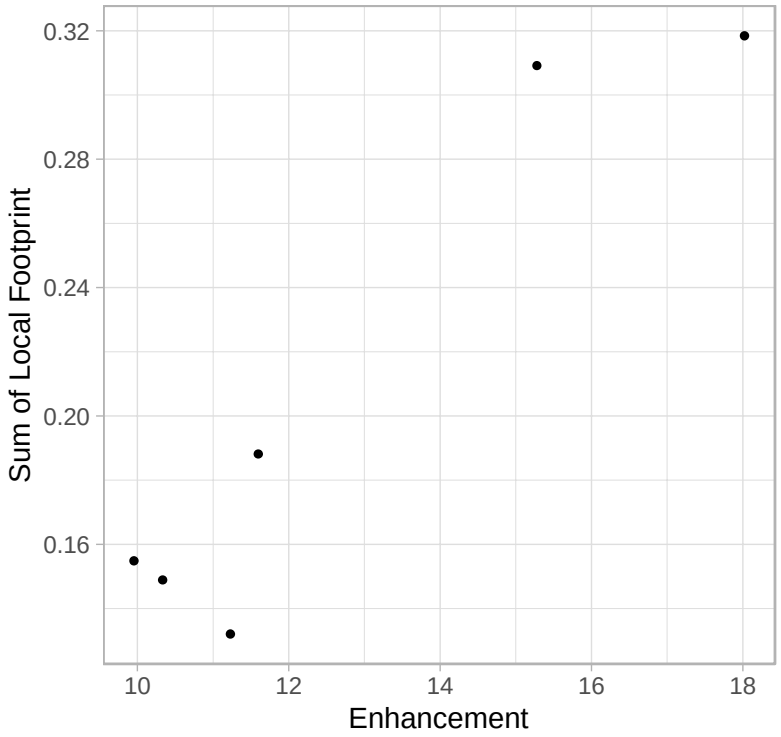

Figure S30. Scatter plot of total modeled enhancement vs. local footprints for GOSAT prototypical location 2 (West Kansas)

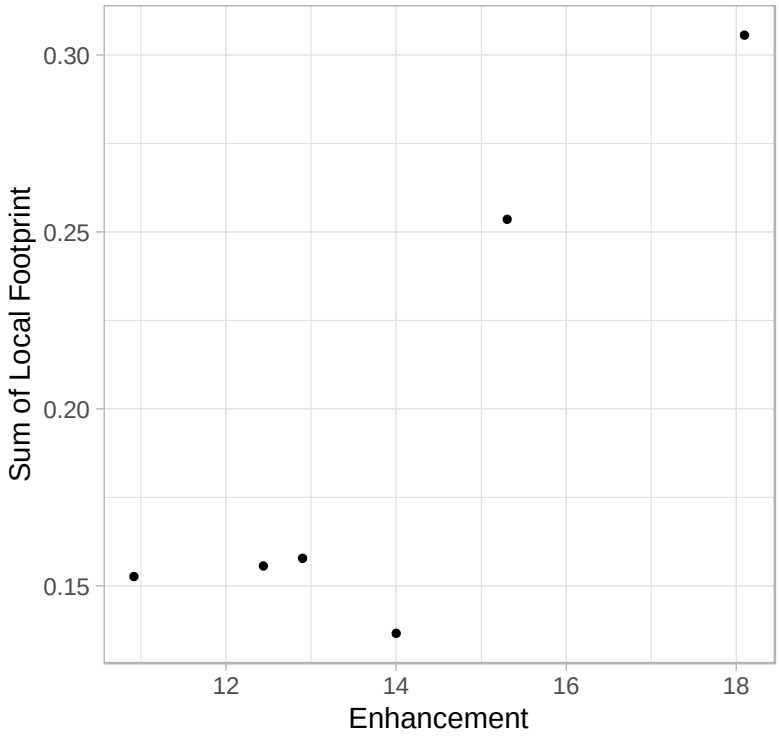

Figure S31. Scatter plot of total modeled enhancement vs. local footprints for GOSAT prototypical location 3 (East Kansas)

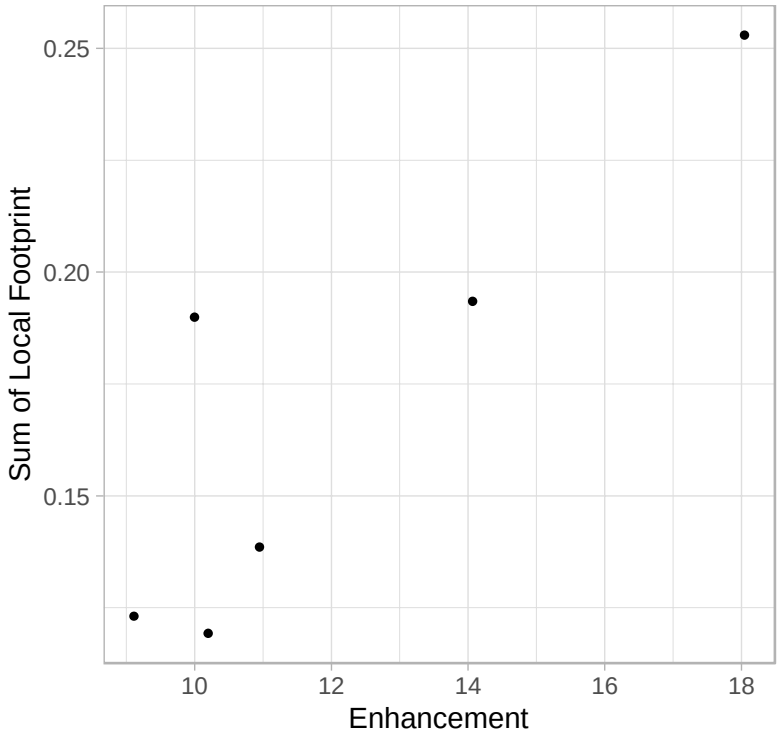

Figure S32. Scatter plot of total modeled enhancement vs. local footprints for GOSAT prototypical location 4 (Chicago area)

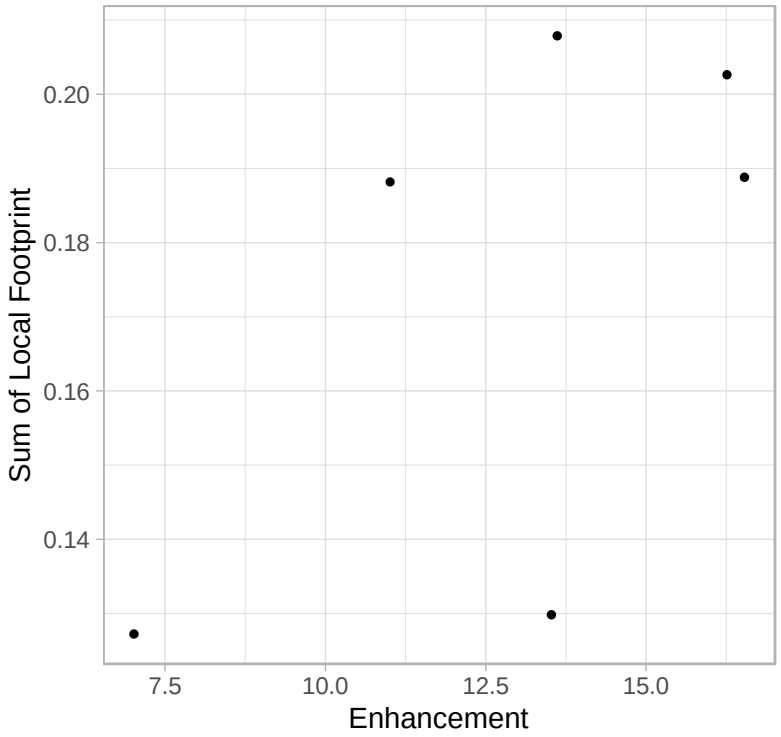

Figure S33. Scatter plot of total modeled enhancement vs. local footprints for GOSAT prototypical location 5 (West New York - West Pennsylvania)

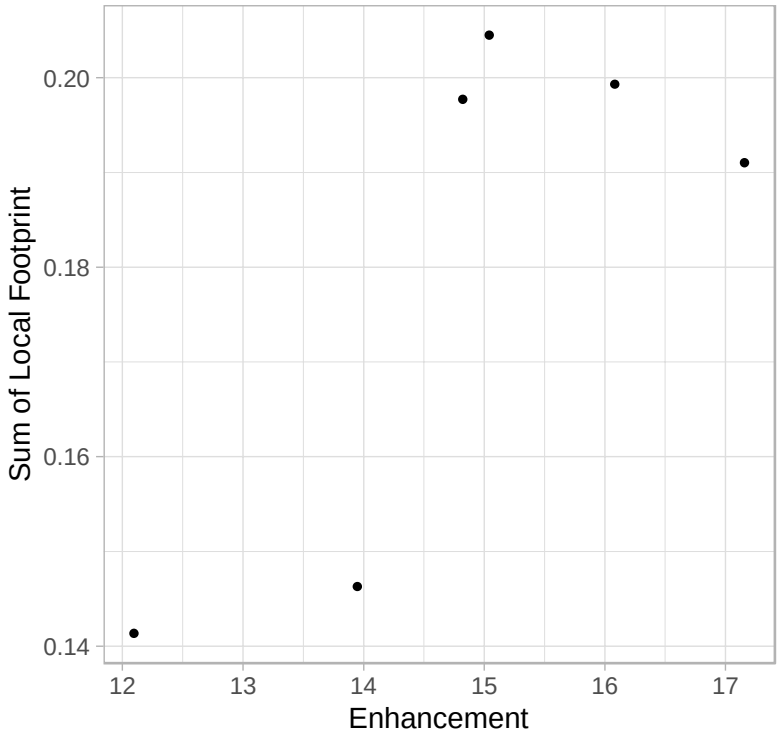

Figure S34. Scatter plot of total modeled enhancement vs. local footprints for GOSAT prototypical location 6 (West Virginia - Southwest Virginia)

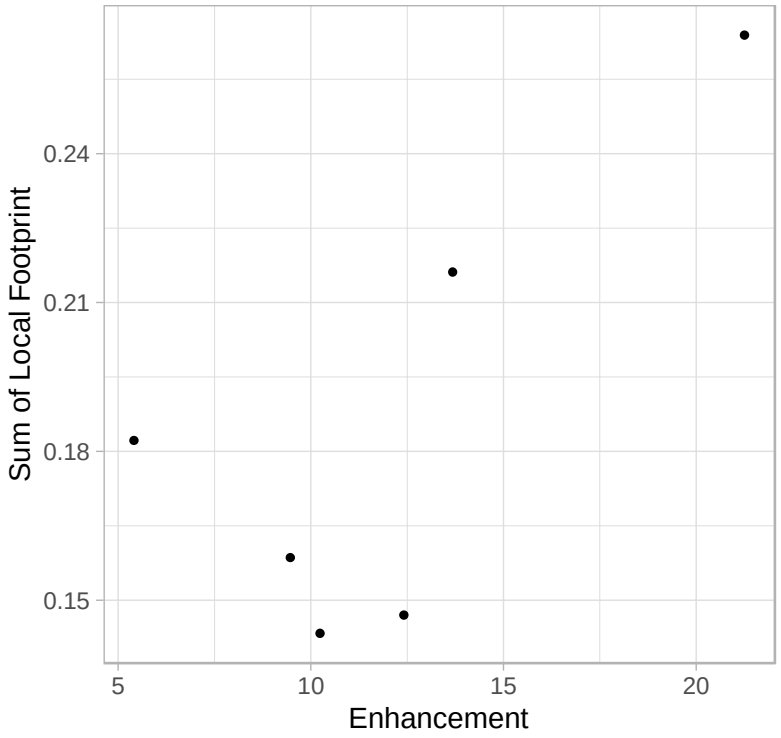

Figure S35. Scatter plot of total modeled enhancement vs. local footprints for GOSAT prototypical location 7 (East New York - East Pennsylvania)

S4 Sensitivity simulations

We conduct two sensitivity tests at sites in oil and gas producing regions (SGP and WKT) to (1) evaluate the sensitivity of the STILT model outputs to the meteorological product used, and (2) investigate possible effects of gaps or irregularities in atmospheric sampling.

For the first sensitivity study, we generate a second set of STILT simulations using meteorology from North American Mesoscale Forecast System 12 km (NAM-12) (NCEP, 2015). We use NAM-12 as an alternative meteorology product in the sensitivity simulation because this product has been used in several existing regional GHG modeling studies (Huang et al. 2019; Ren et al. 2018; Sargent et al. 2021). This product also has a relatively fine spatial resolution (12 km) relative to some other meteorological products, making it a good choice for regional-scale GHG modeling. Figures S32a and S33a show the model simulations using NAM-12. Both figures show the monthly-average MMR (i.e., no methane background or boundary condition added; not de-seasonalized). This setup for Figs. S32-33 allows for a direct visual comparison among the different sets of model outputs.

In both the NAM-12 STILT (Fig. S35a and S36a) and WRF-STILT (Fig. S35c and S36c) simulations, a trend in emissions has a small impact on the overall modeled timeseries. For example, the differences between S1 and S3 are small relative to overall variability in

MMR across both sets of model results. By contrast, we do find that the two models sometimes yield different MMR estimates for individual months. For example, NAM-12 tends to estimate higher peak MMR values relative to WRF simulations. Despite these differences between models, the overall impact of a trend in emissions is similar relative to the overall variability in each timeseries.

We further conduct a sensitivity test to evaluate the possible impacts of irregular sampling on the modeled timeseries. In general, flask samples are collected in the afternoons at each tower site, but there is some variability and gaps in sampling frequency. For example, there are typically 30-40 flasks available per month at WKT in years 2008-2010, but sampling frequency drops to ~10 observations per month in years 2012-2015. There are also individual months with relatively few samples, including September, 2008, which had about a quarter as many observations at WKT compared to surrounding months. In contrast to WKT, SGP consistently has been 4-5 observations per month during the study period.

In this sensitivity test, we compute NAM-12 STILT footprints for 1pm local time each day and construct modeled timeseries based on this output (Figs. S35b and S36b). The timeseries at WKT look nearly identical to one another; the model simulations with a fixed, daily sampling time look very similar to the modeled timeseries using the actual observed sampling times (Figs. S36a-b). By contrast, the simulations at SGP show noticeable differences compared to the timeseries using observed sampling times (Figs. S35a-b). We suspect that the low sampling frequency at SGP yields a monthly-averaged timeseries with high variability; the small number of samples collected each month means that the monthly average can vary greatly from one month to another. By contrast, the timeseries in the fixed experiments displays much less month-to-month variability, likely because there are more model points in each month to average over.

Overall, we conclude that sampling frequency and regularity can have an impact on MMR, particularly when those timeseries are averaged to aggregate timescales (e.g., monthly). With that said, the impact of a trend in emissions is small in all cases relative to overall monthly variability in MMR (e.g., S1 versus S3 in Figs. S35-36).

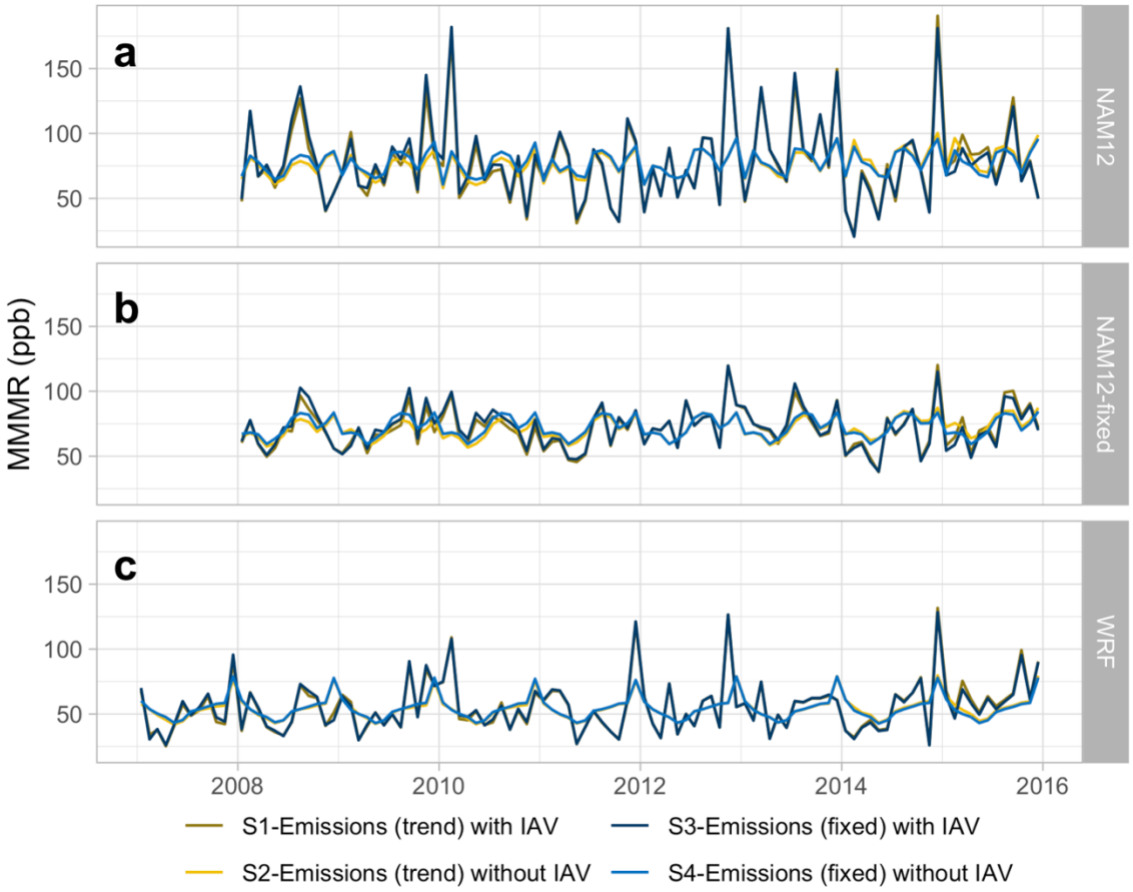

Figure S36. Comparison between monthly averaged MMR timeseries at site SGP for all 4 modeling scenarios using NAM12, NAM12 with fixed sampling time, and WRF meteorology products

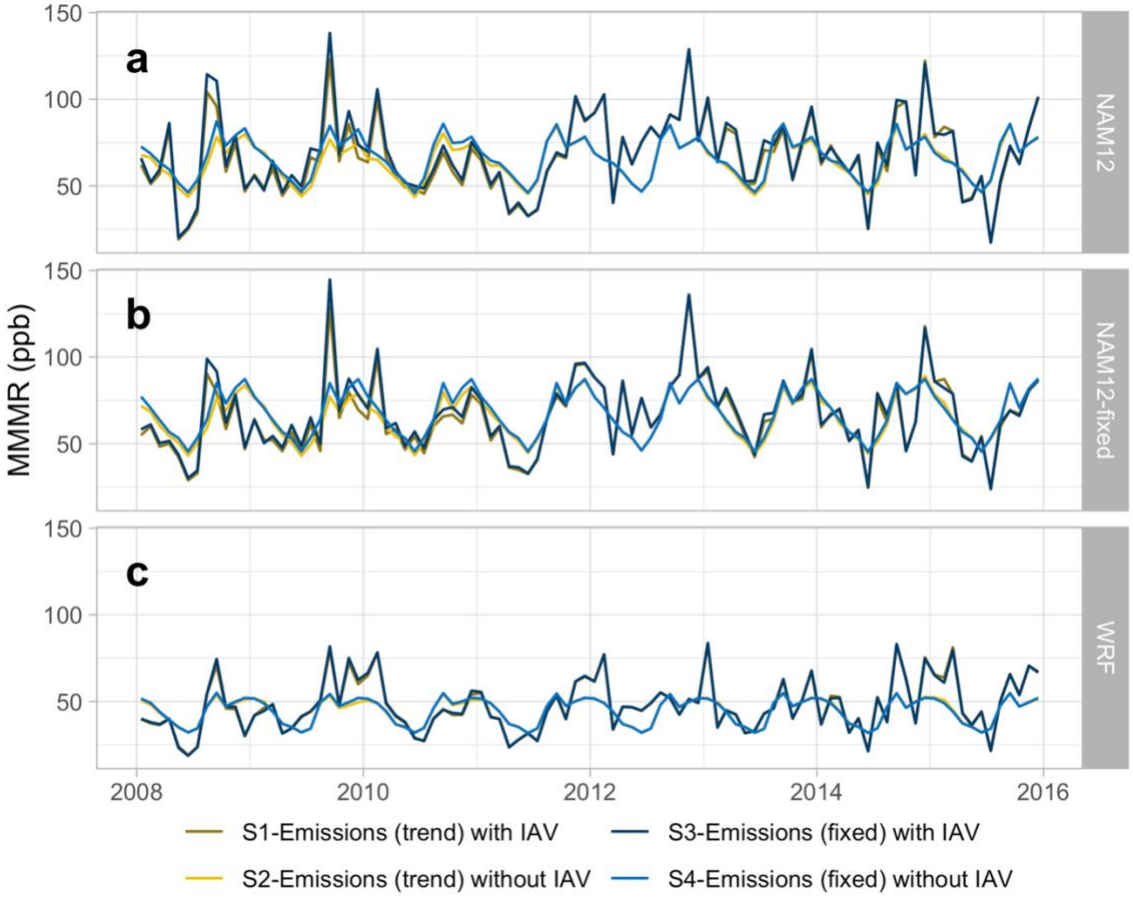

Figure S37. Comparison between monthly averaged MMR timeseries at site WKT for all 4 modeling scenarios using NAM12, NAM12 with fixed sampling time, and WRF meteorology products